Theses and Dissertations

Spring 2014

Understanding mechanical trade-offs in changing centers of rotation for reverse shoulder arthroplasty design

Vijay Niels Permeswaran
University of Iowa

Recommended Citation

Permeswaran, Vijay Niels. "Understanding mechanical trade-offs in changing centers of rotation for reverse shoulder arthroplasty design." MS (Master of Science) thesis, University of Iowa, 2014.
http://ir.uiowa.edu/etd/4716.

UNDERSTANDING MECHANICAL TRADE-OFFS IN CHANGING CENTERS OF

ROTATION FOR REVERSE SHOULDER ARTHROPLASTY DESIGN

by

Vijay Niels Permeswaran

A thesis submitted in partial fulfillment
of the requirements for the Master of
Science degree in Biomedical Engineering
in the Graduate College of
The University of Iowa

May 2014

Thesis Supervisor: Associate Professor Donald D Anderson

Graduate College
The University of Iowa
Iowa City, Iowa

CERTIFICATE OF APPROVAL

_____

MASTER'S THESIS

_____

This is to certify that the Master's thesis of

Vijay Niels Permeswaran

has been approved by the Examining Committee
for the thesis requirement for the Master of Science
degree in Biomedical Engineering at the May 2014 graduation.

Thesis Committee: _____
                   Donald D Anderson, Thesis Supervisor

                   _____
                   Jessica E Goetz

                   _____
                   Carolyn M Hettrich

                   _____
                   Nicole Grosland

                   _____
                   Thomas D Brown

ACKNOWLEDGMENTS

TABLE OF CONTENTS

iii

LIST OF FIGURES

CHAPTER 1

INTRODUCTION

<u>Shoulder Anatomy and Biomechanics</u>

Shoulder Structure

The shoulder has oftentimes been called the most complicated joint in the human body. One aspect of the shoulder that makes it difficult to study is that it involves not simply one articulation, but five, including the sternoclavicular joint between the sternum and clavicle, the acromioclavicular joint between the acromion process of the scapula and the clavicle, the coracoclavicular joint between the coracoid process of the scapula and the clavicle, the glenohumeral joint between the glenoid surface of the scapula and the humerus, and the scapulothoracic joint between the body of the scapula and the thoracic cavity. Furthermore, with the exception of the coracoclavicular joint, each of these joints experiences significant rotation during even simple arm motions. The joint most often studied, as well as the joint directly affected during shoulder arthroplasty, is the glenohumeral articulation [1].

Many types of rotation occur at the glenohumeral joint, including flexion, extension, frontal plane abduction and adduction, horizontal abduction and adduction, and internal and external rotation. In addition, due to the limited conformity of the glenoid surface, the humerus is also capable of translating across the glenoid surface. Finally, in contrast to other joints, there is a large surface area mismatch between the glenoid surface and the humeral head, with the humeral head articulating surface encompassing nearly four times the area of the glenoid. Due to this relative lack of inherent bony conformity/stability, the glenohumeral joint is the most unconstrained joint in the human body [1].
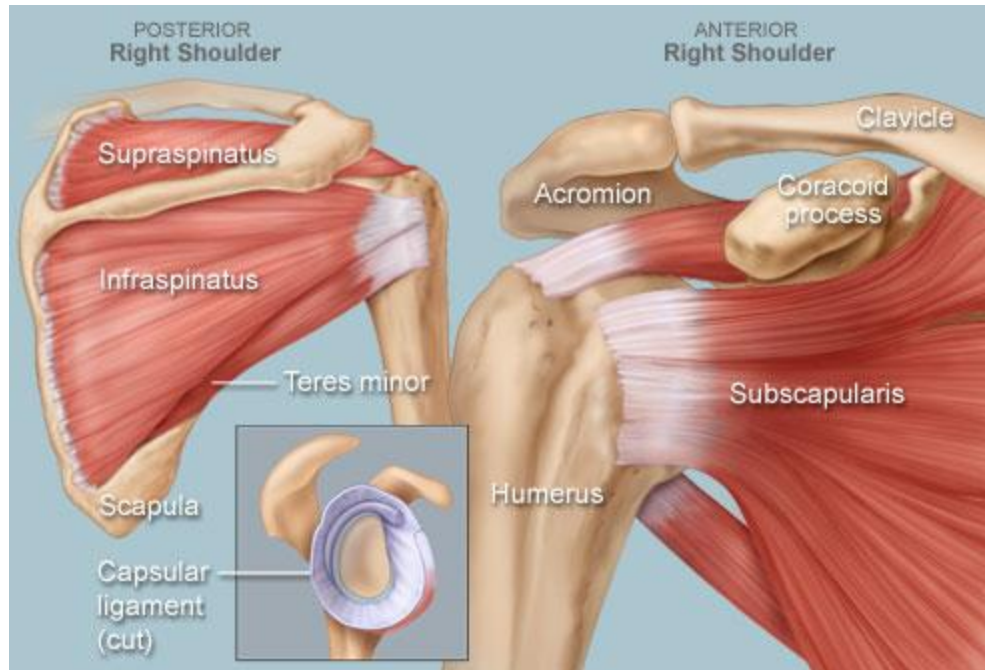
Figure 1-1 Anatomy of the human shoulder. Bones include the clavicle, the acromion and the coracoid process of the scapula, and the humerus. The origins and insertions of several rotator cuff muscles (supraspinatus, infraspinatus, subscapularis, teres minor) are also shown. The glenoid surface and capsular ligaments are shown in the inset. Taken from WebMD.

Glenohumeral Capsule Anatomy

Several soft tissue structures help provide support to the shoulder. The glenoid labrum lines the periphery of the glenoid surface, increasing the depth of the articulation between the humeral head and the shallow glenoid. In addition, the ligaments comprising the joint capsule, the superior glenohumeral, middle glenohumeral, and the inferior glenohumeral ligaments, also provide support to the relatively unconstrained glenohumeral articulation. These ligaments are located on the anterior side of the joint, and each provides specialized stability. The taut superior glenohumeral ligament, for example, limits anterior translation and inferior subluxation when the arm is in an adducted state [2-4].

Rotator Cuff Description

In addition to the previously mentioned ligaments, the glenohumeral capsule is also comprised of the tendons of the rotator cuff muscles. The rotator cuff muscles are the supraspinatus, infraspinatus, and teres minor, which are responsible for external rotation, and the subscapularis, which is responsible for internal rotation [5]. However, the rotator cuff muscles play a much larger role than just controlling rotation of the humerus. Because the tendons of these muscles are incorporated into the joint capsule, contraction of the rotator cuff muscles provides added stability to the glenohumeral joint. Before any motion of the humerus occurs, the rotator cuff muscles contract and thereby restrict translation of the humeral head. Through careful and concerted activation of these muscles, the joint is able to achieve stability [1].

Motion of the Shoulder Complex

In contrast to other extremity joints such as the knee or hip, active movement of the humerus is accompanied by passive motion of all five related shoulder articulations. When the upper extremity is elevated, rotation occurs not only between the humerus and glenoid surface, but also between the scapula, thoracic cavity, and clavicle. During frontal plane elevation or abduction, the humerus and scapula both rotate upwards in a coupled motion called scapulohumeral rhythm, commonly defined as the ratio of scapulothoracic rotation to glenohumeral rotation. Although shoulder complex motion varies between individuals, earlier research and observations have established that the first 30° of shoulder abduction is largely glenohumeral, while for shoulder abduction between 30°-90° the scapulohumeral rhythm is 1:2 [6]. After 90°, the greater tuberosity of the humerus approaches and occasionally impinges on the acromion process of the scapula, and any additional arm abduction is achieved through scapulothoracic rotation. In general, the shoulder is a complicated joint capable of complex motions with relatively little inherent bony or passive soft tissue stability.[1, 6].

A Brief History on the Treatment of Cuff Tear Arthropathy

Societal Impact of Cuff Tear Arthropathy

The stability, function, and health of the glenohumeral joint are highly dependent on an intact rotator cuff. Conversely, a damaged rotator cuff can compromise stability of the joint and lead to degradation. Unfortunately, rotator cuff tears are the most common shoulder injury, leading to 4.5 million patient visits a year in the United States and costing society nearly $3.5 billion a year when not treated properly [7-9]. The burden of rotator cuff tears is likely even higher, since many of these tears are asymptomatic and go unreported [7, 8]. Although it is not fully known what causes these asymptomatic tears to progress to symptomatic presentation, much is known of the resulting joint disease known as cuff tear arthropathy (CTA) [10].

Formal Definition of Cuff Tear Arthropathy

Neer et al. first fully reported on CTA in 1983 [10]. The pathology of CTA starts with a massive rotator cuff tear. The cuff tear leads to instability of the glenohumeral joint, which allows the humeral head to migrate superiorly into the subacromional space, even at rest. Uneven loading of the articulating surface leads to glenoid cartilage, and eventually bone, destruction, usually classified simply as osteoarthritis or OA. Symptoms of CTA include pain, reduced range of motion, reduced shoulder function, and in some cases pseudoparalysis (small or no active range of motion but full passive range of motion) of the shoulder joint (Figure 1-2). Prior to Neer's report, several competing theories about the origin of CTA existed, including mechanical compression of the rotator cuff tendons under the coracoacromial arch, intrinsic changes to the tendon composition, as well calcium phosphate crystals inducing an immunologic cascade, leading to cartilage degradation [11-14]. Neer et al.'s work is widely acknowledged as the definitive explanation of the progression of cuff tear arthropathy from asymptomatic to symptomatic.

Figure 1-2 Frontal and lateral views of patient with CTA and pseudoparalysis (right arm). Patient exhibits stark difference in range of motion between diseased and healthy shoulder. Taken from Gerber et al. 2009.

Traditional Treatments and Issues of Cuff Tear Arthropathy

Total Shoulder Arthroplasty

Many forms of treatment for CTA were suggested at the time of Neer's report. Total shoulder arthroplasty (TSA) had already been documented as a satisfactory solution for glenohumeral arthritis in the absence of other shoulder diseases [15]. However TSA was found to be inadequate for shoulders without a functional rotator cuff. In patients with CTA, the constraint usually provided by a healthy rotator cuff is absent, and, while TSA resolves the problem of cartilage degradation, it does not restore stability [16]. Without this stability, shoulder function does not return, because muscle contraction produces humeral translation rather than rotation. The best form of treatment was described as extremely difficult and required a TSA to restore the bearing surface plus rotator cuff reconstruction to restore joint stability [10, 12].

<u>Glenohumeral Arthrodesis</u>

Another option for treating CTA is glenohumeral arthrodesis (fusion). In a glenohumeral arthrodesis, the humerus and scapula are fused together using internal fixation (i.e., plates and screws). The goal of this procedure is to reduce pain by eliminating motion at the joint [17]. However, arthrodesis patients suffer from many complications. Due to poor bone quality remaining at the joint, there is a high rate of non-union. In addition, well-fused joints usually encourage increased scapulothoracic motion, leading to pain [17, 18].
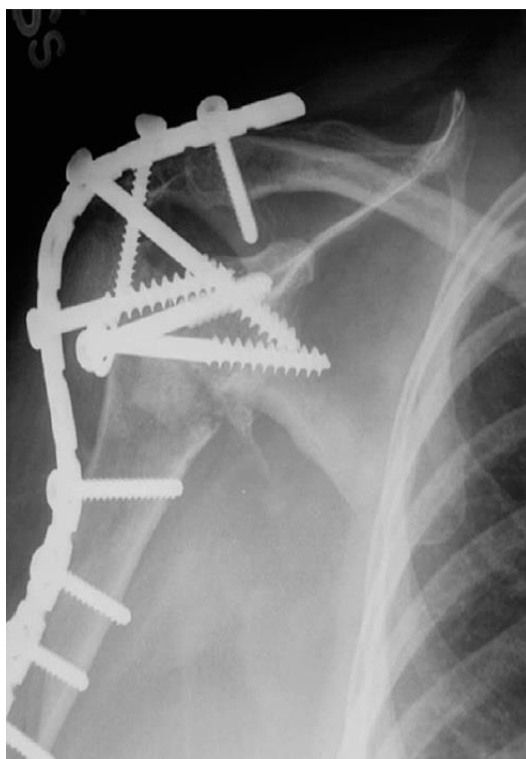
Figure 1-3 Frontal plane radiograph of shoulder arthrodesis. The purpose of the implanted construct is to prevent any motion of the humerus relative to the scapula, fixing the glenohumeral joint. Taken from Nam et al. 2010.

Shoulder Hemiarthroplasty

Upon the advent of the hemiarthroplasty, these implants were also proposed for treating CTA. Hemiarthroplasty involves removing only one side of the joint, instead of all articulating surfaces; in the case of shoulder hemiarthroplasty, only the humeral head is replaced with an artificial implant [11, 13, 14, 18, 19]. Although these procedures produced good clinical results initially, hemiarthroplasties eventually were subject to instability in patients with CTA. As described by Sanchez-Sotelo et al. in 2001, "Although shoulder hemiarthroplasty is not a perfect solution for patients with glenohumeral arthritis and severe cuff deficiency, it probably represents the best available reconstructive option for this difficult problem at the present time" [18].

Instability and the Rocking Horse Phenomenon

Hemiarthroplasty and TSA experience the same problem in CTA patients. In glenohumeral joints with OA and healthy soft tissue, the capsule and rotator cuff provide support and stability, allowing motion of the joint, and replacement of the bearing surface relieves pain. However, in CTA patients, the replacement of the bearing surface does not solve the inherent problem of instability and reduced shoulder function and range of motion. Without an intact rotator cuff, the humeral head is prone to translation with respect to the glenoid surface. Rotator cuff deficiency prevents the humeral head from sustaining a stable center of rotation, the deltoid muscle pulls superiorly, causing the humeral head to translate across the glenoid surface to achieve rotation rather than rotate smoothly. This instability of the humeral head is associated with cartilage and bone degradation in the native shoulder and baseplate loosening and fixation failure in TSA-reconstructed shoulders [20]. In TSA, uneven loading of the glenoid surface creates a superior tipping of the component, often known in the field as the "Rocking Horse Phenomenon" [11, 13, 14, 16, 21].
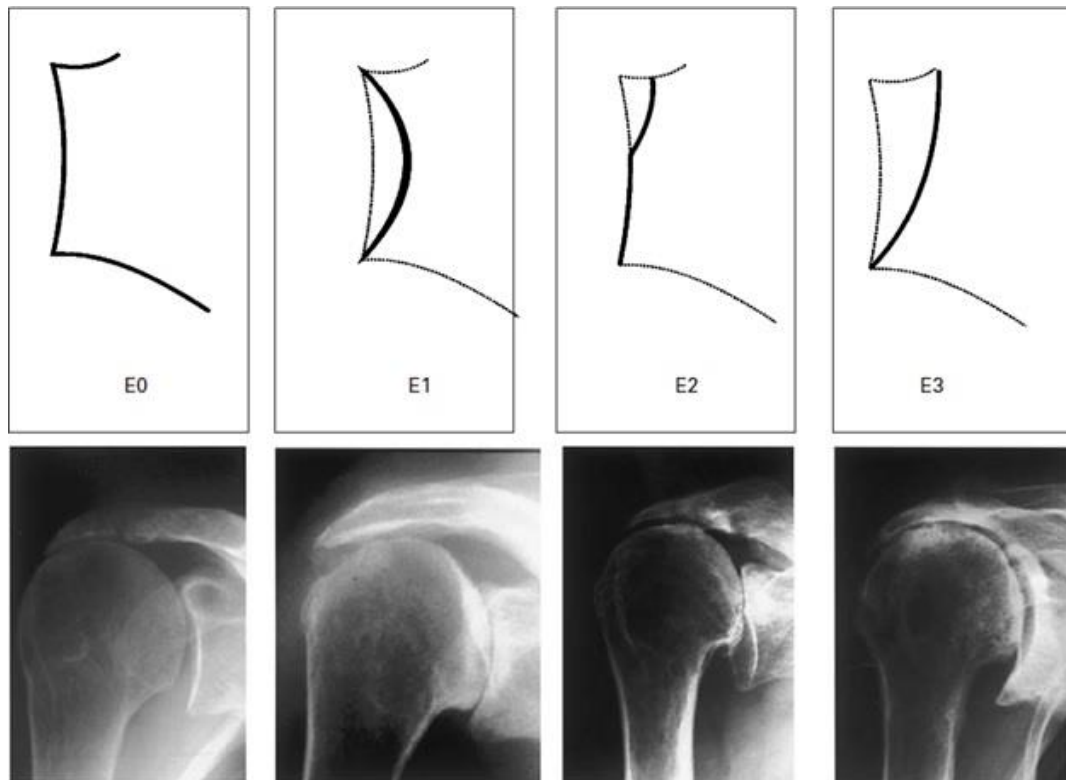
Figure 1-4 Glenoid erosion classifications and corresponding radiographs. As humeral superior loading increases, glenoid cartilage and bone degradation intensifies. Taken from Sirveaux et al. 2004.

Reverse Shoulder Arthroplasty

Development and History

In order to solve the many complications associated with arthroplasty in shoulders with CTA (e.g. glenoid component loosening and failure, as well as loss of motion) a new prosthesis was designed. In 1985, Grammont et al. introduced the first modern reverse shoulder arthroplasty (RSA) [16, 19, 22]. This first design consisted of a metal or ceramic prosthesis that was two-thirds of a 42 mm diameter sphere, which was implanted into the glenoid surface, and an all-polyethylene trumpet-shaped component which was cemented in the humerus [16].

In this design, the joint structure was reversed compared to the native shoulder; the native concave glenoid surface is replaced by a convex glenosphere, and the native convex humeral head is replaced by a humeral implant with a concave polyethylene cup. After variable range-of-motion results were seen in the first 8 patients, Grammont decided to alter the design [16]. The new design, the Delta III released in Europe in 1996 by DePuy (DePuy Synthes, Warsaw, Indiana), incorporated five parts including a glenoid baseplate, a glenoid hemisphere or glenosphere, a polyethylene bearing surface, a humeral neck, and a humeral stem [16].

Figure 1-5 Exploded view of components in the DePuy Delta III reverse shoulder prosthesis designed by Grammont. Taken from Wierks et al. 2009.

Design and Design Rationale

Many alternative designs have been proposed, but most reverse RSA designs share the same principles. The glenosphere is implanted into the scapula, facilitating a

stable center of rotation along with the supporting musculature between the scapula and thoracic cavity. Also, the implantation technique suggests planing or smoothing the glenoid into a flat surface, placing the glenosphere and therefore the center of rotation more medially and oftentimes inferiorly compared to the native shoulder [12, 14, 16, 19]. This inferior placement stretches and pretensions the deltoid, providing greater joint stability. In addition, the medialization of the center of rotation increases the effective moment arm of the deltoid. This increase in moment arm helps the deltoid achieve greater active range of motion and shoulder function [23]. Finally, the stable center of rotation can provide resistance to superior translation of the humerus, preventing uneven loading and the rocking horse phenomenon from developing in the glenosphere [11, 14, 16]. Following RSA, favorable outcomes in restoring range of motion and shoulder function have been reported [11, 13, 14, 16, 19, 20, 22-26].

Scapular Notching

Definition of Scapular Notching

Despite their many potential benefits, RSAs are difficult to perform properly, leading to complication rates as high as 23% with reoperation rates as high as 12% [11, 14, 16, 19, 20, 22-24, 26-28]. The most common complication is scapular notching, which is seen in as many as 96% of cases in one study. Scapular notching occurs when bone on the scapular neck inferior to the glenosphere is resorbed or worn away due to impingement by the humeral polyethylene cup [11, 14, 16, 19, 20, 22-24, 26, 27]. It is not yet fully understood whether or not bony resorption or fragmentation is the primary mechanism whereby scapular notching occurs.
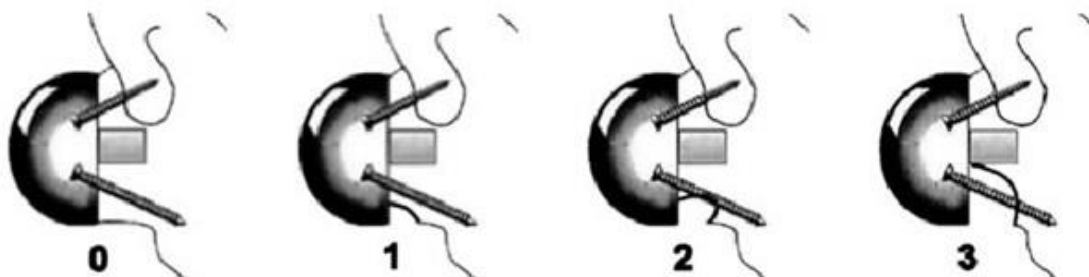
Figure 1-6 Diagram of the progression of scapular notching. The far left image shows no erosion of the inferior glenoid region and the far right shows a scapular notch progressing past the inferior fixation screw and approaching the central peg of the baseplate. Taken from (Boileau et al. 2006)
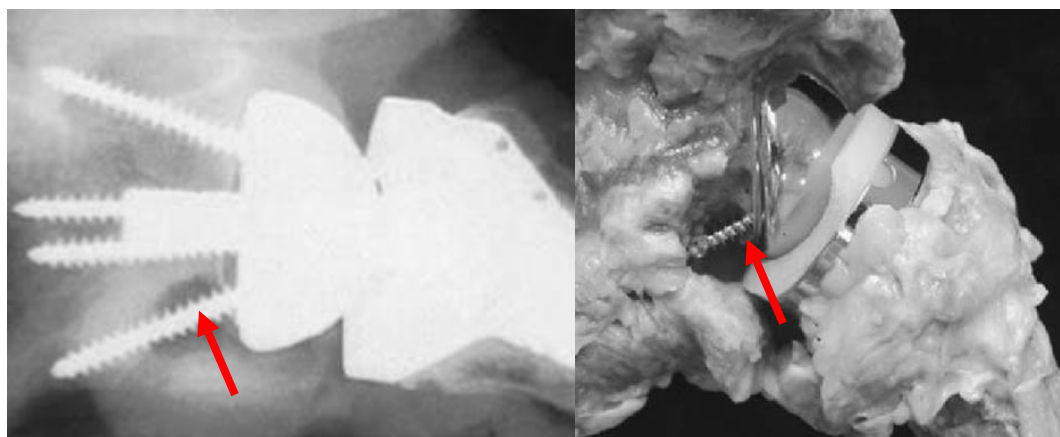
Figure 1-7 Radiograph and ex-vivo image of shoulder retrieval experiencing scapular notching. The arrow shows scapular notching as evidenced by radiolucency present near the inferior screw region denoting bone loss. In the right image, the arrow points to the area of scapular notching with the fixation screws visible. In addition, not seen in the radiograph, the polyethylene cup has been significantly damaged from repetitive contact with the exposed screw. Taken from Nyffeler et al. 2004.

Current Techniques to Prevent Scapular Notching

Several different implantation options have been used to prevent scapular impingement. One concept involves implanting the glenosphere with some inferior overhang rather than centrally on the glenoid surface [23, 29-32]. By placing the

glenosphere inferiorly, the patient is afforded more humeral adduction before impingement between the humeral component and the scapular neck. Another implantation option is the bony increased offset (BIO) method [33]. In the BIO method, a small cylindrical disc of bone harvested from the humeral head is implanted between the planed glenosphere and the glenosphere baseplate [33].

The BIO implantation has several attractive features. First, the lateralization increases the range of motion before impingement between the humeral cup and scapula. Second, the lateralization is achieved via addition of existing bone and not through addition of excess metal. This is beneficial because the humeral bone oftentimes grows into the scapula, providing extra fixation for the glenosphere in the narrow scapula. Importantly, the center of rotation of the joint remains at the implant-bone interface, rather than in the center of the implant (Figure 1-8). This nullifies the potential for a torque or moment at the fixation site by eliminating the lever arm of the reaction force.

Inferior overhang and BIO are just two techniques that have been proposed to address the problem of scapular notching. Others options include changing humeral neck-shaft angle, humeral version, glenosphere version, and implant size. Currently, there is debate regarding which technique, as well as implant system, produces the best clinical results [33-40]. Finite element analysis and other computational modeling techniques provide a means whereby biomechanics can be used to discern trends and relationships between the many variables involved and, eventually, provide a firm basis for improving clinical results.
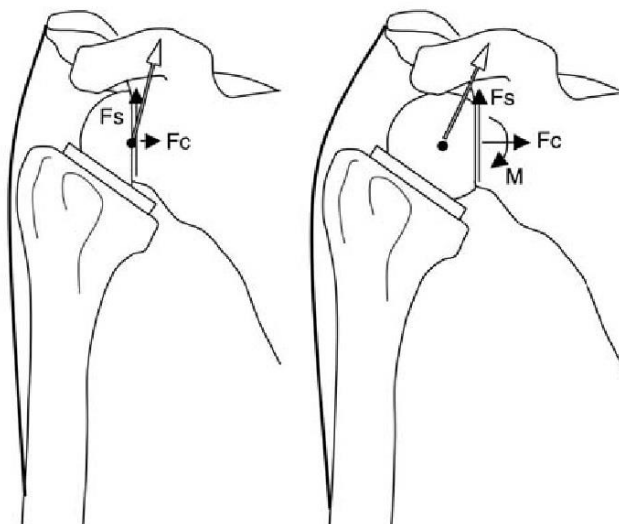
Figure 1-8 Partial free body diagram of two different RSA techniques. Fc is the compressive component of the joint load, Fs is the shear component of the joint load, and M is the moment created by the joint load. In the left implantation, there is no distance between the center of rotation and the fixation, eliminating a joint reaction moment. The right implantation separates the center of rotation from the fixation site, creating a potentially unstable joint reaction torque. Taken from (Gerber et al. 2009).
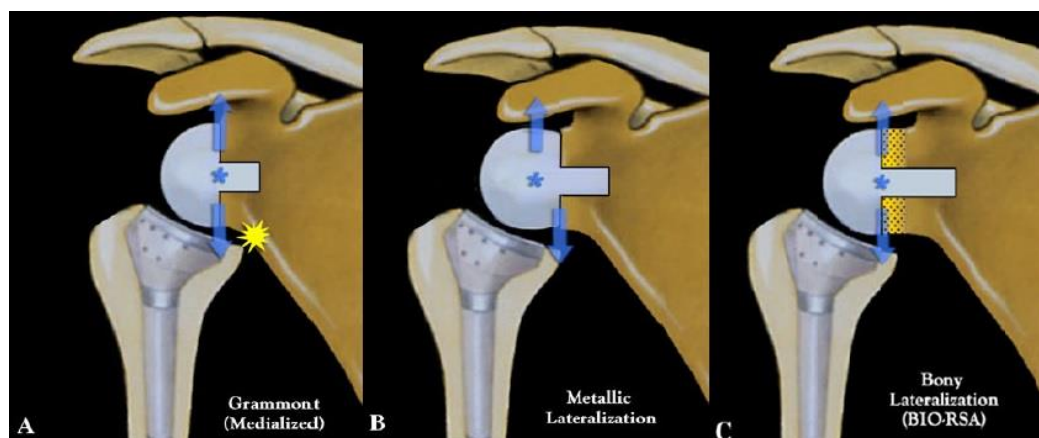
Figure 1-9 Three common implantations of RSA. A displays the most common implantation of early RSA. Impingement is expected for this type of implantation as shown with the yellow explosion symbol. B shows a metallic lateralization technique where the center of rotation is lateralized through a glenoid implant that is greater than a hemisphere. C shows a BIO-RSA lateralization technique. The center of rotation is lateralized through implantation of a bone graft behind the glenoid baseplate. Taken from (Boileau et al. 2011).

Brief Overview of the Finite Element Method

Theory of the Finite Element Method

The Finite Element Method (FEM) has revolutionized the engineering field. From aviation to thermodynamics to orthopedics, few if any fields can say they have not employed FEM to analyze design. The basic process of the FEM encompasses computing deformations and stresses by solving a series of equations.

First, the laws of physics are broken down into their respective governing partial differential equations (PDEs). These PDEs are called the strong form in FEM. These strong form equations are very difficult, if not impossible, to solve analytically for complex geometry. Therefore, the strong form equations are combined with weighting functions to produce integrals known as the weak form equations. In the weak form, the equations are only valid in certain domains specified by the integration limits. In the weak form, the equation is simply an integral over the domain. The solution of this integral is the amount of external virtual work done on the system. However, the solutions of interest are the displacements of the model at specific points on the body called nodes. From these displacements, stress and strains can be calculated. In order to find the displacements, the weak form equations are broken down using weighting and interpolating functions. These functions interpolate the displacement values between nodes. In addition to these functions, the constitutive relationship matrix of the material is introduced to produce linear equations that are assembled into a matrix, known as the global stiffness matrix, where the connectivity of all nodes is defined. The displacement of the nodes are then solved using a numerical solver [41].

Therefore, there are two steps of the FEM where the solution is approximated. First, the solution is approximated when the global strong form equation is limited to the weak form domain. Second, when the weak form is transformed into a series of linear equations, the solution is approximated at specific point called mesh points or nodes.

Finally, the solution to the matrix equations is not solved analytically but numerically in real-world geometries [41].

Historical Development of Finite Element Method

FEM was developed during the 1950s, and the theory and process were described in four seminal papers published during that era. In the first of these papers, Courant solved St. Venant's torsion of a square hollow box by minimizing a stress function on the external boundary using linear approximation between discrete points [42]. These discrete points became the precursor to modern nodes. Next, Argyris used a matrix theory of structures, where he defined discrete elements instead of weak form integrals. He combined these discrete elements and matrix theory to define the first stiffness matrices. Using the stiffness matrix formulation, he solved a rectangular panel plane stress problem [42]. The work by Turner introduced the truss element, where member areas are incorporated into the equations, as opposed to one-dimensional elements with no cross sectional area modeled. Also, Turner proposed the first triangular element, as opposed to rectangular elements. In addition, he was the first to define the elements in relation to the global axes rather than axes local to the elements, in addition to incorporating these global coordinates into the stiffness matrix. Finally, Clough is credited with validating the FEM. He found that for higher mesh densities, the solution Turner detailed converged towards the known analytical solution for a particular geometry. Clough is also the inventor of the name "finite element method" [42].

Early Orthopaedics Models

Soon after the FEM was accepted as a valid computational tool, it was embraced by the field of orthopedics. In 1972, the first use of the FEM in orthopedics was published by Brekelmans et al., in which they used FE to analyze the mechanical behavior of "skeletal parts" [43]. Subsequently, many studies were conducted to analyze bone stresses. However, the true explosion of the FEM in orthopaedics coincided with the

large increase in volume of arthroplasties performed in the late 1970's and early 1980's. In order to improve clinical outcomes, orthopedic implants were modeled to better understand the mechanical failures experienced and to increase the functional life of the devices. The first and still the most commonly modeled anatomic site was the hip, a result of the thriving total hip replacement field. Initial models were relatively crude utilizing linear elasticity, isotropic bone material properties, and idealized two-dimensional, axisymmetric, or non-specific smoothed three-dimensional bone and implant geometries [43].

Finite Element Modeling of the Shoulder and Shoulder Arthroplasty

Early Shoulder Models

The shoulder and shoulder arthroplasty hardware were first analyzed using FEM in the late 1980's. In the first series of finite element shoulder models, two dimensional FE models of the glenoid were created to analyze the change in stresses experienced by bone before and after implantation with keeled or and pegged glenoid baseplate designs for total shoulder arthroplasty [44]. That same work also included a model of the humerus which was created to study the stress difference between two types of humeral implant fixation [44].

Modern Shoulder Models

Native Shoulder FE Models

More complex three-dimensional FE and non-FE computational models of the shoulder were developed in the 2000s. One of the earliest efforts to model the native shoulder in 3-D was reported by Buchler at al. in 2002. That model used spring elements to hold the scapula fixed and the humerus in stable position during loading. Also, two sets of muscle elements, representing the subscapularis and infraspinatus, were created to

provide internal or external rotation loads on the humerus. In order to produce each motion, the muscle responsible for that motion was pre-stressed by displacing the insertion site medially while fixing the humerus. Motion was produced when the humerus was allowed to rotate along its long axis. Using this approach, a model with healthy cartilage was compared to an osteoarthritic shoulder with no cartilage, and higher contact stress was found on the glenoid surface in the OA model as opposed to the healthy shoulder [45].

In 2007, Terrier et al. added more sets of muscles to the model seen in Buchler et al. 2002. In the Buchler et al. 2002 model, only two muscles were incorporated. In addition, the muscles had no active elements and required pre-stressing to generate motion. In the model presented by Terrier et al., all rotator cuff muscles (supraspinatus, infraspinatus, subscapularis, and teres minor) as well as the three heads of the deltoid were modeled. The muscles were modeled with a series of passive elements and user-defined active cable elements with logic for muscle shortening. Humeral abduction motion was driven with these muscle elements. The model showed that uneven glenoid contact and superior migration of the humerus occurred when abduction was achieved in the absence of a supraspinatus [46]. The most notable features of these two studies are the muscle elements with passive and active components. Rather than using kinematic constraints to drive shoulder motion, the motion of these models was driven kinetically with muscle forces. This approach is important in the shoulder where the competency or deficiency of soft tissues structures such as the capsule and rotator cuff muscles have a key role in determining motion, as opposed to the hip where bony congruity is the leading contributor to femoral motion
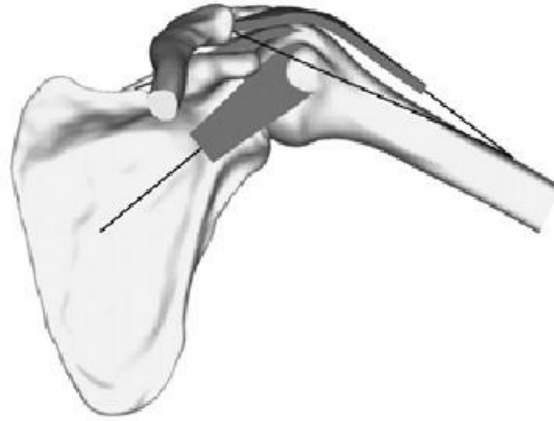
Figure 1-10 Diagram of 3-D model of native shoulder. In the model, muscles were modeled with passive continuum elements (shown in the figure as ribbons) and active cable elements (shown in the figure as lines). Mentioned above, loading of the shoulder is done ideally through muscle and soft tissue modeling instead of joint positions. Using muscle elements with passive and active elements allows modeling the shoulder in this way. Taken from Terrier et al. 2007.

In addition to the soft tissue of the rotator cuff, efforts have been made to model the glenohumeral capsule. In 2010, Ellis et al. used a validated subject-specific FE model of a humerus, scapula, and shoulder capsule to assess the ability of different clinical tests to evaluate capsule integrity [47]. The bones were modeled as rigid bodies, and the cartilage was modeled using shell elements. The majority of complexity in the model involved the material properties of the capsule. Rigorous material testing provided hypoelastic isotropic material models for specific regions of the capsule. Results found higher strains on the glenoid side of the joint as opposed to the humeral side, and that some clinical tests may not be adequate to test humeral-side capsule strength, as strains were inconsistent in that region [47]. In 2011, Drury et al. used the same model and found high correlation of strain in the anterior-inferior capsule of two different subject-specific capsule models [48]. The soft tissue and capsular modeling in these studies is

very detailed. These models demonstrate that the material properties of the glenohumeral capsule can be measured quantitatively and used to produce accurate results in a finite element model.
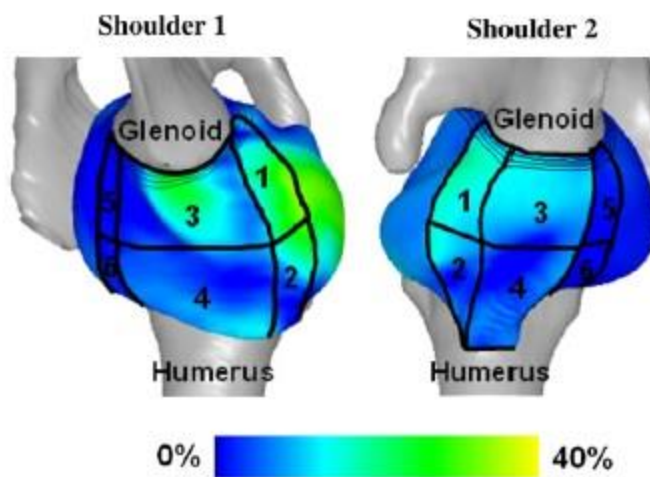
Figure 1-11 Inferior view of strain for two patient specific finite element shoulder capsule models. This model divided the capsule into 6 sub-regions of the inferior capsule. These images show similar regions of strain for both models. The effort required to create patient-specific geometry and region-specific material properties is noteworthy. Taken from Drury et al. 2011.

Total Shoulder Arthroplasty FE Models

There are also many published studies describing the development and use of FE models of total shoulder arthroplasty (TSA). The majority of clinical complications after TSA are fixation failure on the glenoid side. Therefore, the majority of FE models developed in the 2000s focused on glenoid fixation parameters, such as cement mantle and fixation design. In 2000, Lacroix et al. published a FE model studying different types of fixation in TSA, specifically the stress in the cement mantle for pegged and keeled glenoid plate fixations in healthy and osteoarthritic bone. Lower stress values were found using the pegged design in normal bone, and lower stress was found for keeled design in

arthritic bone [49]. These results suggest that bone quality and material properties are important when studying fixation. Furthermore, modeling of implant fixation may require bony geometry from CTA patients to enhance accuracy.

In 2001, Couteau et al. modeled TSA to study stress in the cement mantle around the glenoid baseplate and validated the model using a cadaveric shoulder, strain gauges and pressure sensitive film. This group found higher stress in the cement mantle with off-center loads as opposed to central loads [50]. Terrier et al.'s work predicted uneven glenoid loading with incomplete or missing rotator cuff muscles. Couteau et al.'s results show that uneven loading is a problem, as increases in fixation stress are seen with off-center loads.

In 2005, Hopkins et al. published on the necessity of modeling the entire scapula with muscles in TSA studies. The group concluded that a complete shoulder model should be created when studying fixation, but modeling only a region of the scapula is acceptable when studying the implant systems [51]. Using these results, Hopkins et al. asserted that studying range of motion or implant contact can be calculated with only a glenoid model. In 2006, Hopkins et al. published on a validation of a model studying dislocation in TSA. Four fixation designs were modeled including two pegged designs with different backside geometries (curved vs. flat) and two keeled design with different conformities (perfectly conforming and under conforming). Dislocation forces and displacements were recorded for all glenoid designs. Models were found to correspond very well to a similar physical model. Dislocation forces were similar across all designs, but the keeled conforming glenoid design allowed half the amount of humeral superior translation as the other designs [52].The results of this study underline the importance of bearing surface conformity on stability. For both of these studies, the importance of geometry is illustrated; whether it is obtaining accurate results for glenoid fixation or studying joint stability, geometry is key.

Similar to Couteau et al.'s work with cement mantles, Mansat et al. published in 2007 on the effect different loading locations has on the cement mantle in TSA. In their study, loading on the superior-anterior or superior-posterior section of the glenoid component was found to more than double the stress seen in the implant and cement mantle as opposed to central loading [53]. Sarah et al. created a two-dimensional finite element model to study fixation of a completely polyethylene glenoid prosthesis, and concluded that efforts to strengthen the cement mantle are misguided, as the site of failure is not in the cement but at the bone cement interface [54].

Terrier et al. published a finite element model of TSA in 2012 studying the effect of polyethylene thickness on muscle forces. Studying changes in center of rotation, Terrier et al. found that thinner polyethylene components effectively medialized the implant, thereby increasing the deltoid muscle moment arm and reducing the muscle force required for abduction, which reduced the joint reaction forces. However, the thinner polyethylene resulted in increased stress in the polyethylene and the cement mantle, while the thicker polyethylene component had opposite effects (decreased muscle moment arms, higher joint reaction forces, lower cement and prosthesis stress) [55].

Overall, the literature of finite element models studying total shoulder arthroplasty shows that finite element models can and have been used to study biomechanics and fixation for arthroplasty in this joint. Also, these models show that the direction of model generation is driven by the prevalence of clinical problems.
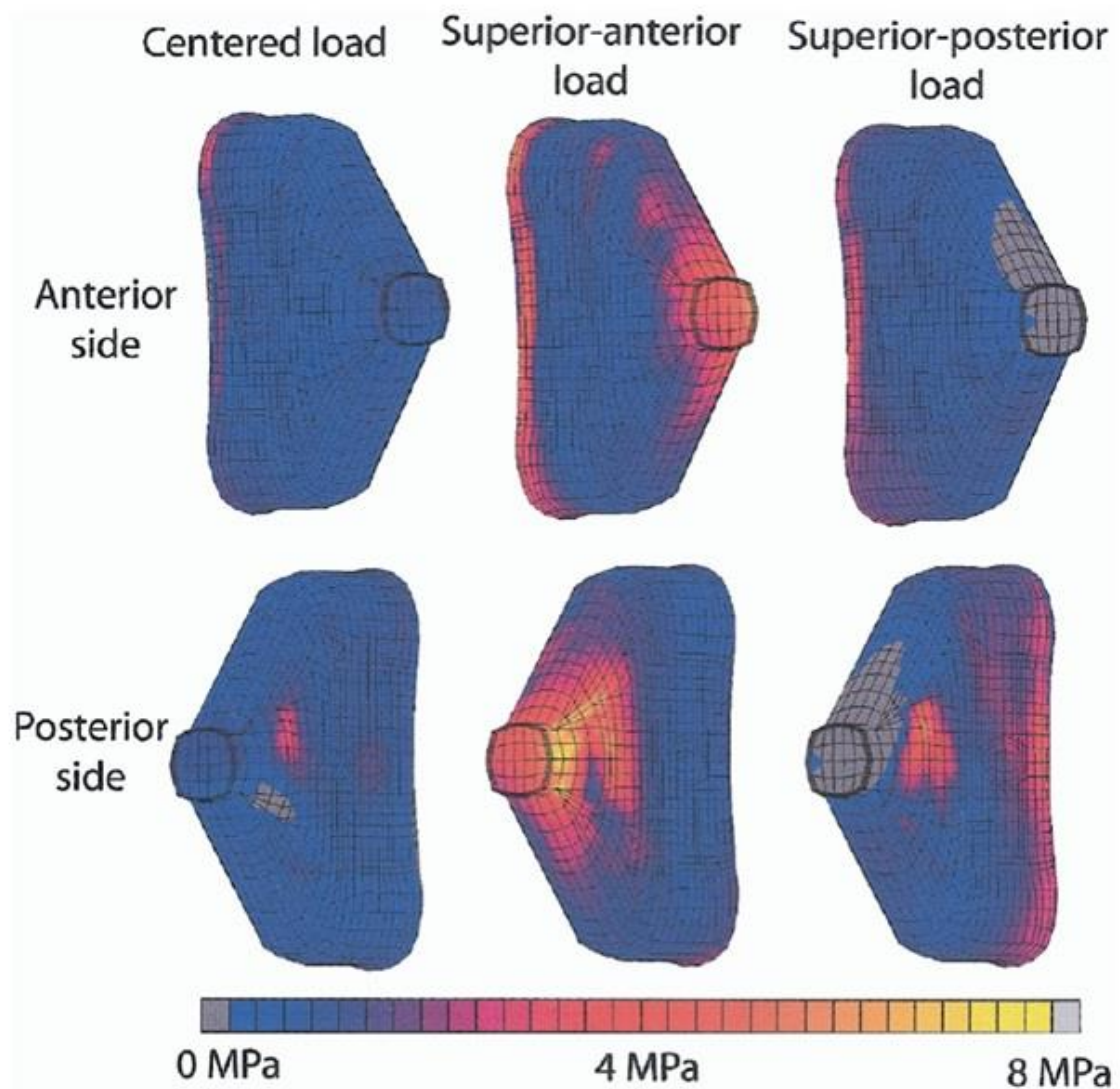
Figure 1-12 Maximum principal stress experienced by the cement mantle behind the glenoid component in TSA. The figure shows anterior and posterior views of the cement mantle of the glenoid component from a medial perspective. Higher stress was seen in superior-anterior and superior-posterior loadings as compared with a centered loading. This figure is an example of the multiple studies published to attempt to understand the complication of glenoid fixation failure. Taken from Mansat et al. 2007.

<u>Reverse Shoulder Arthroplasty Modeling</u>

Reverse Shoulder Arthroplasty Finite Element Models

<u>Finite Element Models Simulating In-Vivo Conditions</u>

Many computational and physical models of RSA have been published. However, due to the fairly recent FDA approval of RSA in 2003, few of these published models are fully defined or validated finite element models with long histories of model progression. In 2004, Ahir et al. published on a FE model of the Bayley-Walker RSA implant system (Stanmore Implants, Elstree, United Kingdom). This implant system was introduced in Europe in the 1980's, and while it shares some features of modern Grammont-style prostheses such as a reverse ball and socket design, it achieves this principle using radically different geometry compared to the DePuy Delta III or Tornier Aequalis (Tornier, Amsterdam, Netherlands) RSA systems (Figure 1-13) [56]. For the model the researchers created, only the glenoid component and scapula were modeled. Static loads were applied through the center of rotation, corresponding to different abduction angles. Higher stress values were found in the implant, as well as at the fixation site when the arm was in 60° of abduction versus 90°. This was attributed to joint reaction forces creating moments within the implant as opposed to purely axial forces at 90° [56]. This study had several limitations. First, the humeral component was not modeled. Because of this, the complex contact and impingement likely to occur were not able to be analyzed. In addition, they used automatic tetrahedral meshes for the scapula and modeled contact between the glenoid component and the scapula. Tetrahedral meshes generally perform poorly in applications involving moving contact. Another limitation was that the mesh had relatively low spatial resolution near the regions of interest, i.e. at the fixation site.

Figure 1-13 Image of Bayley-Walker RSA implant system. The several design differences from the Grammont style design are evident. The polyethylene cup is encased in metal, and the medial edge of the glenosphere does not sit flush with the glenoid bone. Taken from Ahir et al. 2004.

In 2008, Terrier et al. published a model derived from Buchler et al. 2002, discussed in the previous section, to study joint reaction forces and muscle moment arms in RSA versus TSA. That model predicted that RSA implantations increase moment arms of the deltoid muscles while also decreasing the joint force. In addition, the model predicted lower contact forces for a shoulder without a supraspinatus versus a shoulder with one [57]. These results are intuitively reasonable. Discussed in the anatomy section above, the rotator cuff muscles are known to contract and increase joint contact force prior to any motion occurring. Without one of the four rotator cuff muscles, the joint contact force would be expected to decrease.

Yang et al. published a 2-D FE parametric RSA model in 2013. A Tornier Aequalis RSA system was modeled with variations in shape and diameter of the glenosphere, eccentric and central peg locations, thickness of BIO, baseplate tilting angle, and notch severity. For notch severity, the scapular geometry was altered with progressively less bone modeled. Many trends emerged including an increase in stress in the baseplate fixation corresponding with greater eccentricity, and no increase in stress at the fixation site corresponding with increasing notch severity. The study concluded that

inferior fixation screws experience more stress than superior screws. In addition, screw pattern and implantation were found to be more important factors for stress than screw diameter [58]. Although many parameters and factors were analyzed, this model lacks realism due to its two-dimensionality. For all models studied, the geometric cross sections modeled were co-planar, unlike the anatomic joint, where the scapula tilts posteriorly away from the frontal plane. Many of these results would be expected to differ greatly with changes in geometry. In addition, the loading conditions of the humerus were idealized. The weight of the arm was applied to the end of the humerus, and a spring element with a spring constant of 100 N/m was attached to the humerus replicate the deltoid. This static load was used to calculate stress at the implant interface.

Finally, in 2005 Hopkins et al. produced results asserting that a complete scapular mesh is required to study implant fixation. However, Yang et al. only meshed the glenoid region. These studies represent the bulk of in-vivo FE modeling and illustrate the need for more rigorous models with better geometry, loading conditions, and soft tissue incorporated to more fully understand the mechanics at hand.
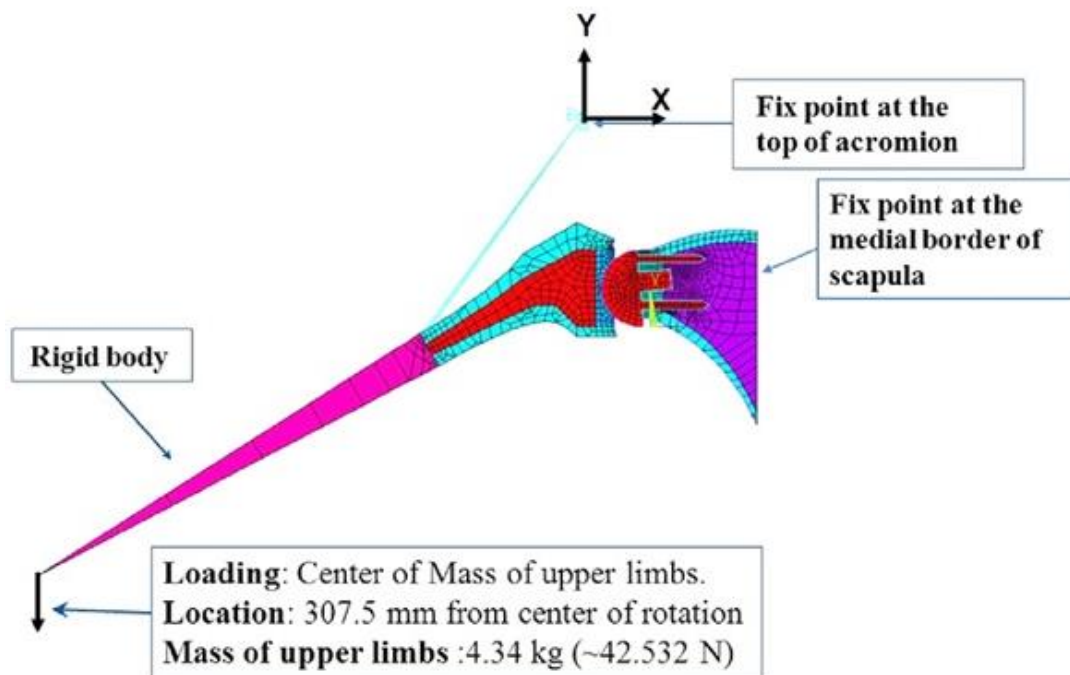
Figure 1-14 Two-dimensional finite element mesh with boundary conditions. The Von
        Mises stress and micromotion was calculated for different parameters
        including glenoid tilt, lateralization, screw placement, glenoid placement, and
        notch severity. In order to study glenoid fixation and other parameters, more
        complex three-dimensional geometry is required, including the entire scapula.
        In addition, more complex dynamic loading is needed. Taken from Yang et al.
        2013

Bench-top Finite Element Models

In addition to in-vivo simulations, a few RSA FE models have been designed to

replicate bench top experiments. A FE model introduced in 2008 was created by Virani et

al. to study baseplate motion in a bench-top setup. The model compared the DJO Reverse

Shoulder Prosthesis (DJO Global LLC, Vista, California) design to the DePuy Delta III

design. The model was validated using physical testing, and results indicated that greater

distance from the center of rotation to the fixation site corresponded to higher baseplate

motion, measured as the displacement of baseplate nodes 3 mm from the baseplate [59].

In general, very few FE models of RSA exist, and many of these models are two-dimensional or contain simplified boundary conditions and geometry.
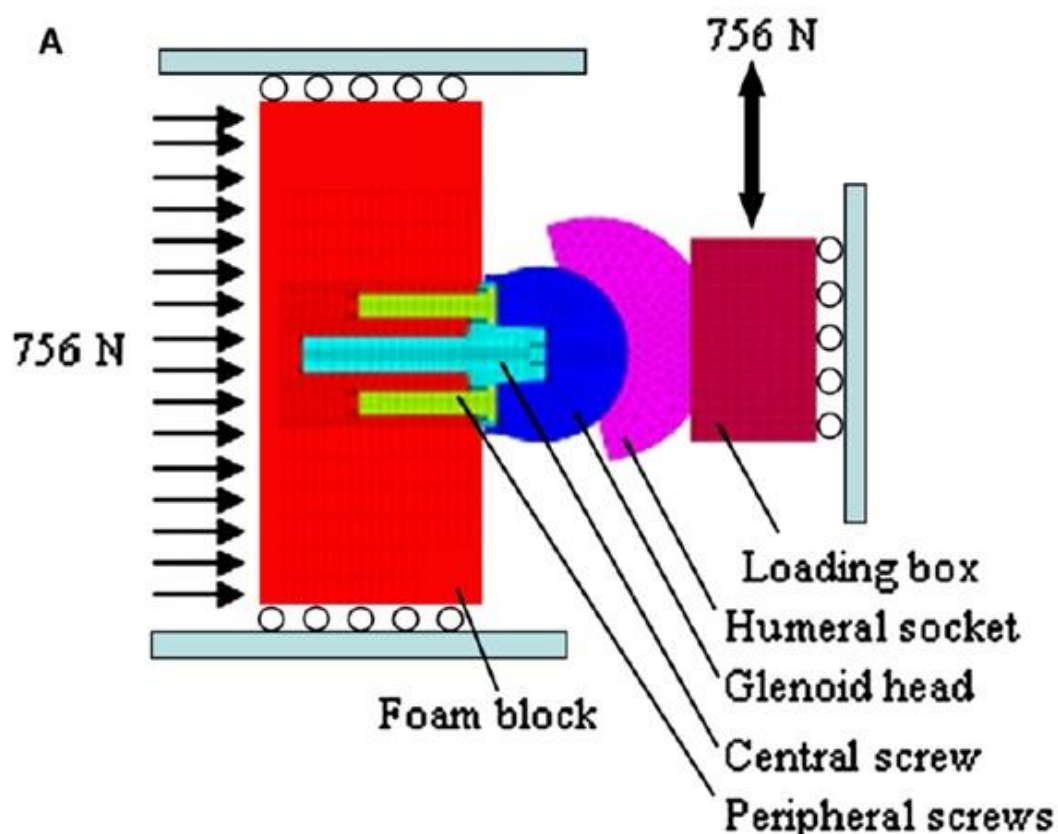
Figure 1-15 Finite element model of fixation testing set-up. DJO RSP geometry is modeled, and the loading conditions are displayed. The model was validated using a physical model. Although these types of model can be used to set-up future studies, more complex geometry is necessary to study micromotion of the baseplate. However, as Hopkins et al. 2005 already reported, studying fixation must be done with the full scapular geometry. The full-thickness foam block used to model bone is not similar enough to the thin cross sections present in the anatomic scapula. Taken from Virani et al 2008.

Reverse Shoulder Arthroplasty Computational Models

For the small number of FE models studying RSA in the literature, a far greater number of non-FE computational models have been published. In 2008, Gutierrez et al.

published a SolidWorks (SolidWorks, Concord, Massachusetts) model which was validated using Sawbones (Pacific Research Laboratories, Vashon, Washington). Those models were used to study which implantation factors have the greatest effect on scapular plane abduction range of motion. Factors modeled included lateralization, superior/inferior position, glenosphere inferior tilt, and humeral neck-shaft angle. Although all factors were found to have some effect, lateralization was found to have the greatest effect on range of motion (ROM), increasing the average ROM across all permutations of implantations with an average of 53.6° for implantations with no lateralization versus an average of 85.5° for implantations with 10 mm of lateralization [60]. Also in 2009, Kontaxis et al. published a combined SIMM (MusculoGraphics, Inc., Santa Rosa, California) and Matlab (MathWorks, Natick, Massachusetts) model studying muscle and joint contact forces in RSA. Using their model, they determined that the humerus translates medially and inferiorly during RSA implantation. Their results also agreed with those reported in Terrier et al. 2008, where joint contact forces decrease from native to RSA [61].

In 2012, Gulotta et al. published a study of the effects of humeral retroversion on internal/external range of motion using a CAD model validated with a cadaveric model. Four levels of retroversion (0°, 20°, 30°, and 40°) were studied. The soft tissue was removed from the cadaveric shoulders, and the muscles were replaced with cables and pulleys. All shoulders were implanted with Biomet (Biomet, Warsaw, Indiana) RSA glenospheres, and CAD models were generated from CT images. Both the physical and computational model results indicate that greater range of motion in scapular plane elevation correlated to greater humeral range of motion in all planes. In addition, greater implant retroversion was found to increase external rotation range of motion but also decrease internal rotation range of motion [62]. In 2013, Terrier et al. published work involving a computational CAD model generated from CT images and virtually implanted with the Aequalis RSA system. The four implantation configurations were

subjected to four everyday activities including hand-to-mouth, combing hair, hand-to-back pocket, and hand-to-opposite shoulder, and impingement was calculated using the "Interference Detection Tool" in SolidWorks The models found the BIO and lateralized implantations to be the best, preventing impingement during all motions. They also concluded that in the implantations in which impingement occurred, the scapular motion necessary for free motion would be less than 10° [63]. In other words, no impingement would occur for these models if the scapula rotated at least 10°.

Recently, Hoenecke et al. published an OpenSim model studying muscle and joint forces experienced during abduction for different types of implantation. Implant positions included a standard inferiorly positioned glenosphere with no lateralization, with several other models varying both superior/inferior position and differing amounts of lateralization achieved through BIO. The standard implantation provided the largest deltoid moment arm, producing the smallest muscle force and joint reaction force. The implantation with 13 mm of lateralization implanted 6 mm superior to the baseline created the smallest deltoid moment arm, producing the largest muscle force and joint reaction force [64]. These results correspond well to traditional mechanical logic. The baseline has a medialized center of rotation with respect to the BIO implantation, and this medialized center of rotation clearly increases the moment arm length, directly affecting the muscle force require to create abduction.

These non-FE models reflect the bulk of the computational modeling that has been done for RSA. Many of these models are highly elaborate with many different implantations, humeral motions and positions, and muscle models. These models are useful for studying the muscle forces, range of motion, and change in muscle moment arms (mechanical advantage) associated with different RSA implantations. However, none of these models include the ability to compute stress or strain at the bone-implant interface or calculate contact stress between the humeral cup and the inferior scapula and glenoid. The values necessary to be calculated are tied to the clinical need. If fixation

failure is occurring, greater need exists for finite element modeling of the bone-implant interface. In RSA, the largest issue is scapular notching. To address this issue, finite element models need to be created to predict range of motion of different implantations, and the contact pressure experienced at the inferior edge of the scapula where notching typically occurs. In addition, validation of these models is required to create faith in the veracity of the model results.
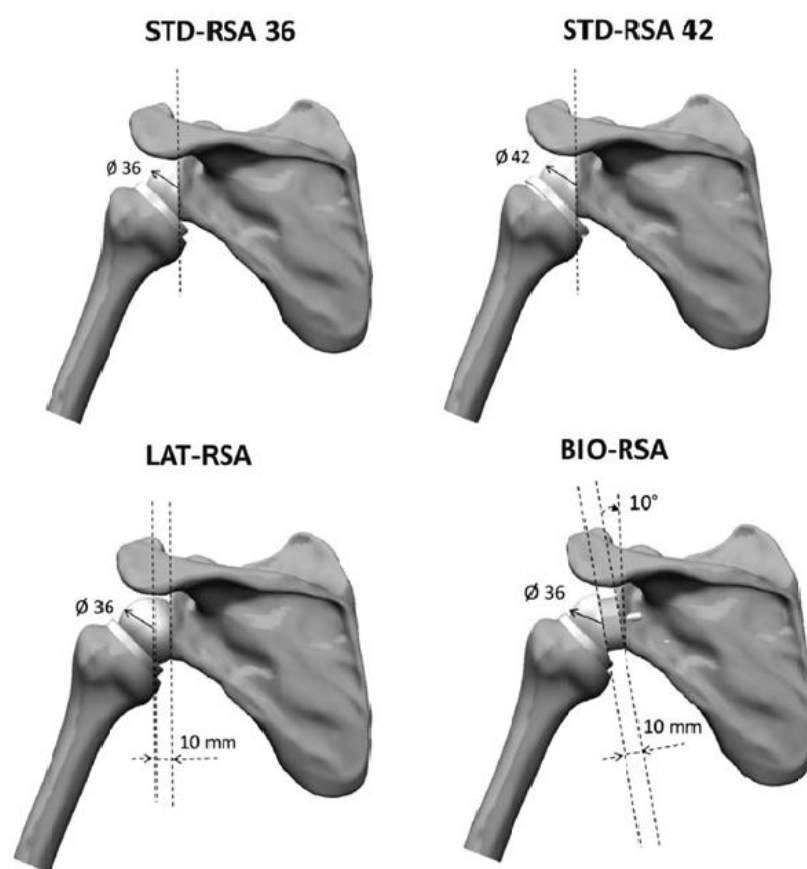
Figure 1-16 Computational models of four different implantation types. In this study, everyday motions were loaded into the models and tested for impingement. Lateralization through implant geometry (LAT-RSA) and BIO-RSA were found to have no impingement for any motion. Taken from (Terrier et al. 2013).

Summary

Though the literature contains many computational models studying RSA, very few utilize finite element analysis to study stresses in the implant and the surrounding bone. The previous sections show that many parameters (center of rotation lateralization, center of rotation superior or inferior position, tilt of the cut glenoid surface, glenosphere shape design, glenosphere size, humeral design, notch severity, etc.) have been studied independently utilizing many different methods (finite element modeling and non-FE computational modeling). However, the previous section also detailed the current limitations in modern modeling as well as many examples of the heights to which finite element modeling can be taken to study RSA. Using these limitations as guidelines, the goal of this project is to create a robust FE model of RSA to study the effect of lateralization on scapular notching and shoulder function.

In the following chapters, the development of the model is detailed. In addition, results produced by the incrementally advanced models are shown. In Chapter 2, the initial finite element model encompassing scapular and RSA hardware geometry is described. Chapter 3 contains description of incremental changes to the model including humeral geometry and muscle element incorporation. An anatomically realistic configuration of the finite element model with increased functionality is detailed in Chapter 4. Finally, Chapter 5 discusses the assets and limitations of the current model as a platform for future research. In addition, a proposed validation protocol is presented.

CHAPTER 2

REVERSE SHOULDER ARTHROPLASTY

FINITE ELEMENT MODEL CREATION

<u>General Model Purpose and Goals</u>

The goal of this portion of the project was to study the effect of changes in implant positioning on contact stress between implant and bone that could explain scapular notching. A finite element model of RSA was first created. The model was developed from Visible Female dataset CT images (Visible Human Project, Bethesda, Maryland) and Tornier Aequalis implant geometry. Virtual implantation was performed with these surface geometries and meshes were developed. Two models were created to study the effect of implant lateralization on range of motion. A medialized model and a lateralized model were loaded to perform adduction until impingement. Then, internal and external rotation, motions thought to promote scapular notching, were modeled with the humerus.

<u>Model Development</u>

Geometric Definitions

<u>Implant Geometry</u>

A Tornier Aequalis Reverse Shoulder Arthroplasty system, (humeral component, glenosphere, and baseplate) was obtained from a company representative, and surface models of the system were generated using a NextEngine 3D Laser Scanner HD (NextEngine, Inc., Santa Monica, California). Due to noise and artifacts from the laser scanning process, the raw surfaces with ripples, spikes, and dimples were unsuitable for meshing. The raw scanned surfaces were imported into Geomagic Studio (Geomagic Solutions, Morrisville, North Carolina), and simple geometric surfaces were fit to selected sections of the laser scanned surfaces to standardize the geometry. A cylinder

was fit to the exterior of the humeral component, two cones were fit to the humeral stem and neck taper, and two spheres were fit to the cup and glenosphere surfaces. These surface geometry parameters were used to create approximated implant geometry. Not all implant features or geometries were analyzed for replication in the finite element mesh. These non-replicated features include the partition between the polyethylene cup and the metal backing, the transition between the neck and stem, and the fin on the neck of the implant for soft tissue attachment. These features were determined to be non-essential for the calculation of range of motion and prediction of scapular notching.

The implant geometry was obtained from a 36 mm implant. For the implants scanned, the diameter of the glenosphere was 36 mm, and the humeral component was perfectly conforming. However, it is more common for a smaller, 29 mm implant to be placed in female patients such as the Visible Female from whom the shoulder geometry was derived. To accommodate this, the humeral cup sphere, cylinder radii, and the glenosphere sphere radius, were scaled to 29 mm. The cone approximating the humeral neck taper was adjusted to have a different height but the same angle, to accommodate the smaller cup diameter. Humerus stem shape parameters were kept fixed to the raw 36 mm scan geometry size.

Raw Scan   Fitted Geometry   Final Geometry
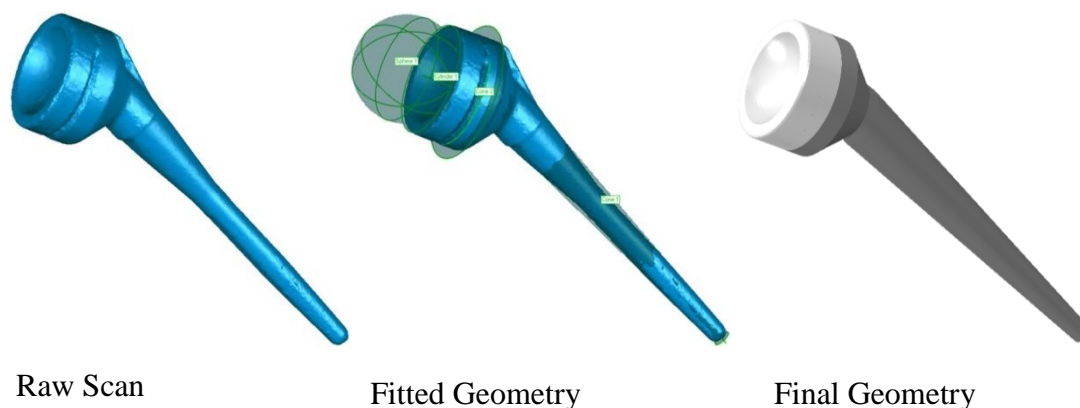
Figure 2-1 Original laser scan geometry, fitted geometry, and finite element mesh created
      from fitted geometric shapes. The original laser scan geometry contains noise.
      A cone was fitted to the stem and neck taper of the laser scan, as well as a
      cylinder to the cup rim and a sphere to the cup itself. These geometries were
      used to define the humeral mesh.

Scapular Geometry

The bony geometry of the scapula was obtained from segmentations of Visible

Female CT images. The edge of the bone was traced in sequential CT slices to generate

.stl surfaces, and the full scapula .stl surface was trimmed in Geomagic Studio to define

only the glenoid region. This was done because understanding scapular notching is the

purpose of this project, and the complex geometry of the bone makes it very challenging

to mesh. The scapular geometry varies greatly, from a relatively circular glenoid to a very

thin wing. In the surface used for meshing, this transition occurred within only two cm of

bone. In Geomagic Studio, all surface points on the glenoid surface were selected, and a

plane was fit to the selection. The best-fit plane captured the normal vector native to the

glenoid surface, or the natural version of the glenoid. A cutting plane parallel to the best-

fit plane was advanced into the body of the scapula until no part of the glenoid surface

intersected the cutting plane. This process mimics the surgical technique. The preparation

of the glenoid surface starts with the surgeon drilling a hole in the center of the glenoid

surface. The drill bit is left in the newly drilled hole and is used as a guide when planing

the glenoid surface.

To separate the glenoid region from the remainder of the scapula, a bounding plane parallel to the cutting plane was offset 25 mm into the body of the scapula. The section of the scapular surface encapsulated by the cutting and bounding plane was used to define the scapular surface for meshing.

The geometry of the BIO cylinder was defined to be the same diameter as the glenosphere baseplate. For the implant system modeled, 29 mm glenosphere implants are implanted with 25 mm diameter baseplates. The thickness of the BIO cylinder was modeled as 8 mm, following with the surgical technique proposed in Boileau et al. 2011 [33]. As opposed to the scapular surface that was manipulated in Geomagic Studio, the BIO cylinder surface was defined completely using primitive geometric surfaces.
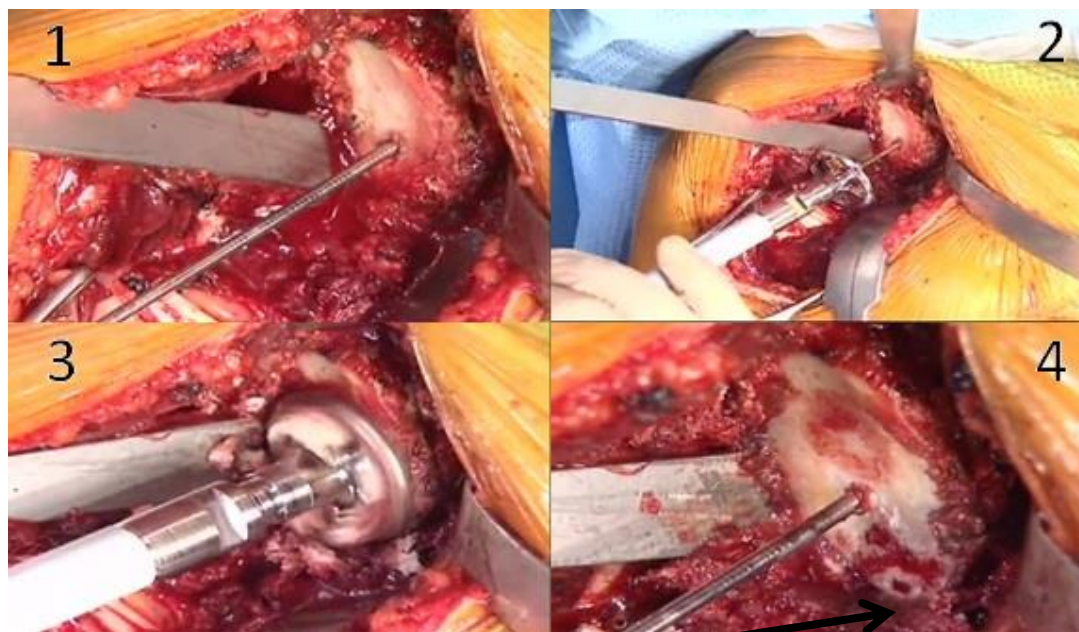
Figure 2-2 Glenoid preparation process. The glenoid is drilled (1), the planer is placed on top of the drill bit (2), the glenoid is planed (3), and the planer is then removed (4). The difference in the glenoid face is seen between the top left and bottom right. The bottom right image depicts a flatter glenoid face with bleeding cancellous bone present in the inferior region, indicated by the black arrow. Taken from Tornier Surgical Technique video 2012 [65].

TrueGrid Description

Basic Meshing Procedure

In order to accurately model contact using finite element analysis, hexahedral mesh generation software was necessary. To fulfill this purpose, all parts of the models were meshed using TrueGrid (XYZ Scientific Applications Inc., Livermore, California). To begin meshing in TrueGrid, a part is defined by the number of "blocks" included in the x, y, and z directions, as well as the number of nodes belonging to the block. Parts are defined individually and can be connected or tied to other parts through block boundary commands. Then, utilizing the projection method, the user projects the faces, edges, or corners of individual blocks in the block structure to model surfaces. Using different block structures and surfaces, a complex mesh can be created by combining the individually meshed parts.

Butterfly Technique

One technique common in projection method meshing is the butterfly. The butterfly mesh technique uses a star or plus-shaped block boundary to define round shapes. With this technique, as opposed to using one block to mesh a round shape, the corner elements are well formed, with less warping and collapse of the element shape, reducing the number of highly acute and obtuse angles in the corner elements.
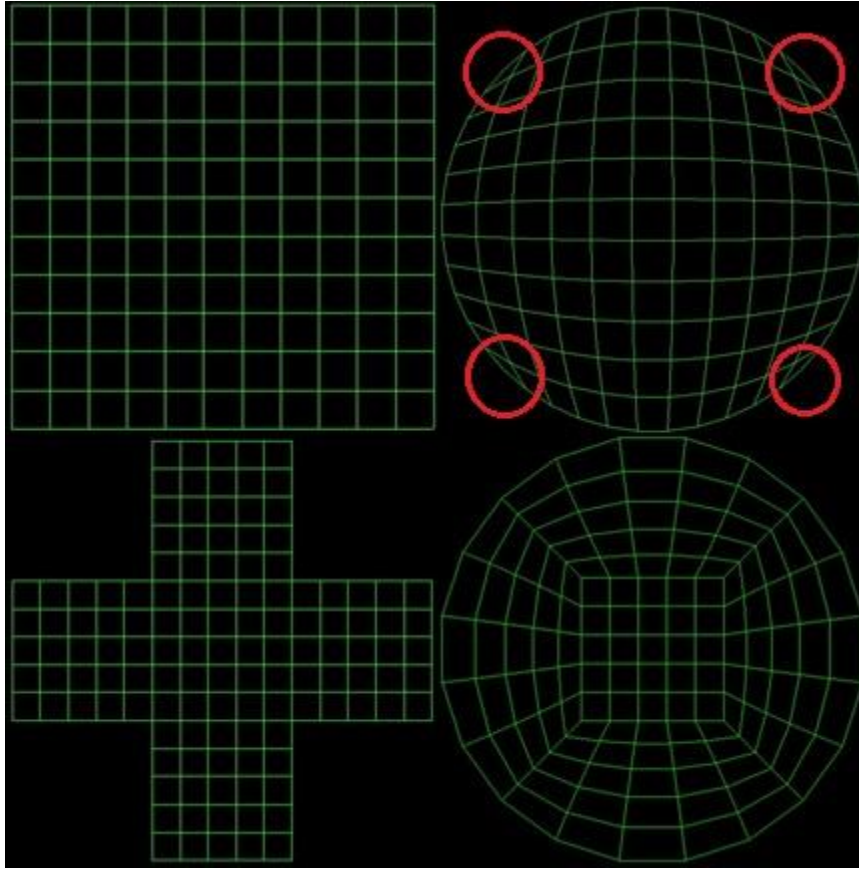
Figure 2-3 FE meshes of a circle created in TrueGrid using two different block structures with similar mesh densities. The left column of images is the block structures before projection, and the right column is the structures after projection. The top row uses one block to approximate a circle while the bottom uses a butterfly technique. The top right image has the poorly formed element on the corners shown in red circles.

Meshing Regimen

The model was meshed in two separate sections, one for the glenoid region and one for the humeral region. The glenoid region mesh started with an initial part for the glenosphere. All parts with surfaces defined by rounded edges, including the glenosphere, glenoid, polyethylene cup, and humeral prosthesis, were meshed using a butterfly geometry technique. The next part meshed was the BIO cylinder. The lateral face of the BIO cylinder was assigned by block boundary to the medial surface of the glenosphere.

Two parts, lateral and medial, were used to mesh the scapula in order to provide greater user ability to match the complex changes in scapular geometry. The lateral surface of the scapula was assigned by block boundary to the medial surface of the BIO cylinder. The model assumed a well-fixed implantation, and no glenosphere fixation was modeled. After all part definitions were created, the parts were merged, and all nodes associated with block boundary assigned surfaces were equivalenced using the surface node tolerance with printout (stp) command in TrueGrid. This commands equivalences all nodes within a tolerance defined by the user. In this case, a small tolerance of .001 mm was chosen to equivalence nodes shared across block boundary assignments.
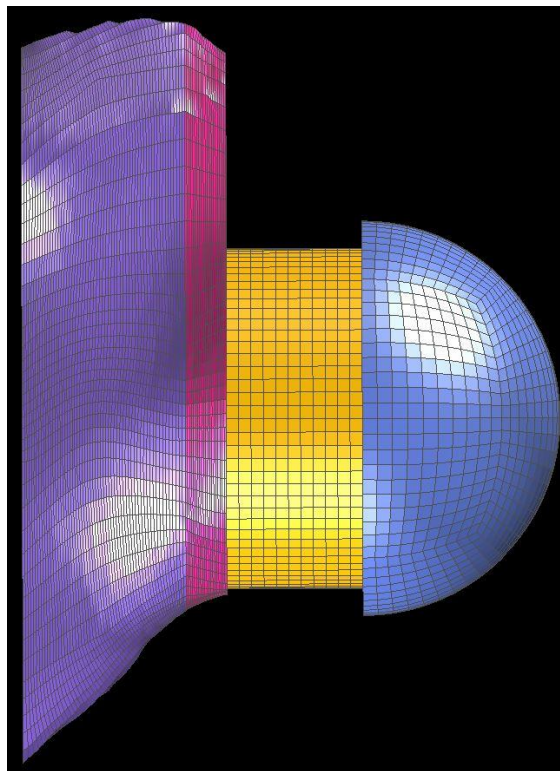
Figure 2-4 Block boundary structure of scapular mesh. Each color represents a different part definition in TrueGrid. The positions of the parts were fixed to each other using the block boundary command. After all part definitions were completed, the stp command was utilized to equivalence nodes across part definitions.

To create the medial model without a BIO cylinder and with a 10° inferior glenoid tilt, the same part procedure was followed, and the same scapular surface was used. Without a BIO modeled, the lateral scapular surface was equivalenced with the medial surface of the glenosphere and the lateral face of the glenoid was projected to a surface rotated 10° instead of completely vertically. The glenosphere was meshed identically first, then locally replicated with a 10° inferior tilt using the local coordinate transform (lct) and local replication (lrep) commands in TrueGrid.

For the humeral region mesh, the cup and cup backing were meshed as one part. For the transition from the humeral cup backing to the stem taper, two parts were utilized. A transition was introduced to reduce mesh density away from the contact areas in order to decrease computation time. After the transition, a new part was used to mesh the taper, and another part was used to mesh the stem. Between all parts of the humeral mesh, a block boundary was used to equivalence the adjoining parts together.

Finite Element Solver Selection

Abaqus/Standard Limitations

All models were run in Abaqus/Explicit. Initial proof-of-concept models with varying amounts of prescribed humeral rotation about simplified glenosphere geometry were run in Abaqus/Standard. However, these original models were unable to compute the contact in an efficient manner. The sliding contact of the humeral cup on the glenosphere as well as the complex contact interactions between the humeral cup and inferior aspect of the scapula created convergence difficulties for Abaqus/Standard. In Abaqus/Standard, the analysis is computed using a Newton method solver. These implicit calculations of the Newton method are computationally expensive but can be used to calculate significantly higher time steps than used in Abaqus/Explicit. However, during complex interactions such as contact and frictional sliding, the Newton solver may not converge. When this happens, Abaqus/Standard cuts back on the time step iteratively

until a convergent solution is found. These time step cutbacks are very computationally expensive and are not guaranteed to ever converge. This issue was discovered during preliminary runs using Abaqus/Standard, as the job would run continually without solution. Guidance from other studies and projects conducted within the Orthopaedic Biomechanics Laboratory was essential to identifying this issue and suggesting alternative techniques [66, 67].

Abaqus/Explicit Advantages

Due to the long run times and oftentimes unstable solutions, the remaining models were run in Abaqus/Explicit rather than Abaqus/Standard. Abaqus/Explicit uses a central difference method to calculate the nodal displacements at every new time step from the nodal velocities and nodal accelerations of the previous time step. The new nodal displacements are used to calculate the nodal accelerations by means of the external and internal forces of the model. Small, computationally inexpensive time steps are used. Comparison of the two methods shows that for models without complex contact, Abaqus/Standard is preferred. However, with complex contact, Abaqus/Explicit is inherently stable and can run models faster.

<center>Model Parameters</center>

Material Properties

The glenoid and BIO cylinder elements were given cortical bone properties (E=15 GPa, v=.3, ρ=1.8 g/cm^3) [45]. As was discussed above, the glenoid section of the bone quickly transitions to thin cross sections of primarily cortical bone. Although some cancellous bone is present in the interior of the glenoid region, cortical bone properties were chosen for all bone elements due to the overwhelming amount of cortical bone in this region. The humeral cup elements were assigned the material properties of conventional Ultra High Molecular Weight Polyethylene (UHMWPE) (E=500 MPa,

v=.4, ρ=.929 g/cm^3) [68, 69], and all metallic implant components were modeled as rigid [67].
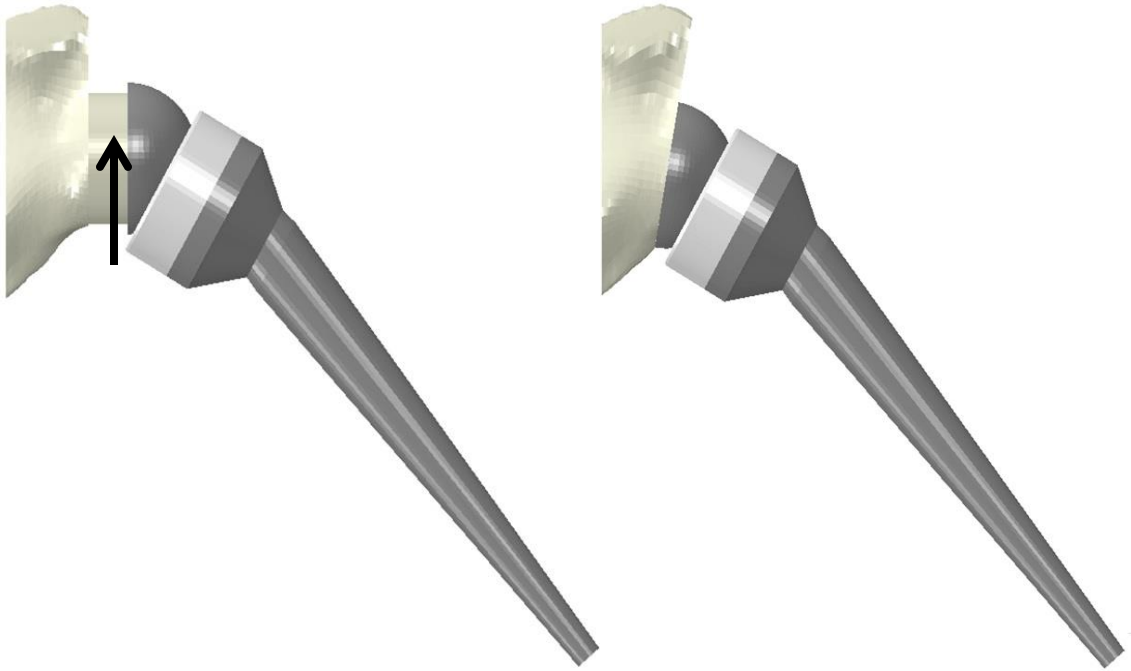
Figure 2-5 Lateralized (left) and medialized (right) models. The lateralized model and is created with an 8 mm BIO cylinder, indicated by the black arrow. The medialized model is created by a 10° inferior cut of the glenoid surface.

Loading Conditions and Outputs Measured

For both models, a moment-generating load was applied at the end of the stem equivalent to the moment generated by the 40 N weight of the average human arm acting at the center of mass of the human arm. The moment was calculated to be 13400 Nmm using anthropometric data [70]. An equivalent moment was created by applying a 92 N vertical load at the end of the stem, 145.7 mm from the center of rotation. To counteract the increase in applied forces, a 52 N upward load was placed at the center of rotation. With this loading scenario, both the forces and moments were equal between the FE and anatomic situations. Adduction deficit, also known as impingement angle, was

determined by starting the humeral component in 40° of frontal plane abduction, fixing

the humeral component center of rotation to the center of the glenosphere, and allowing

the humerus to adduct until impingement of the humeral cup on the scapula occurred.

The humeral component was then fixed in that position, and internally and externally

rotated using an 8500 Nmm force couple moment. Internal and external rotation was

modeled to simulate arm motion likely to cause the highest stresses at the impingement

site, and therefore create the most scapular notching. This type of loading condition

would occur in vivo during many everyday activities such as using a computer mouse or

threading a belt through pants.
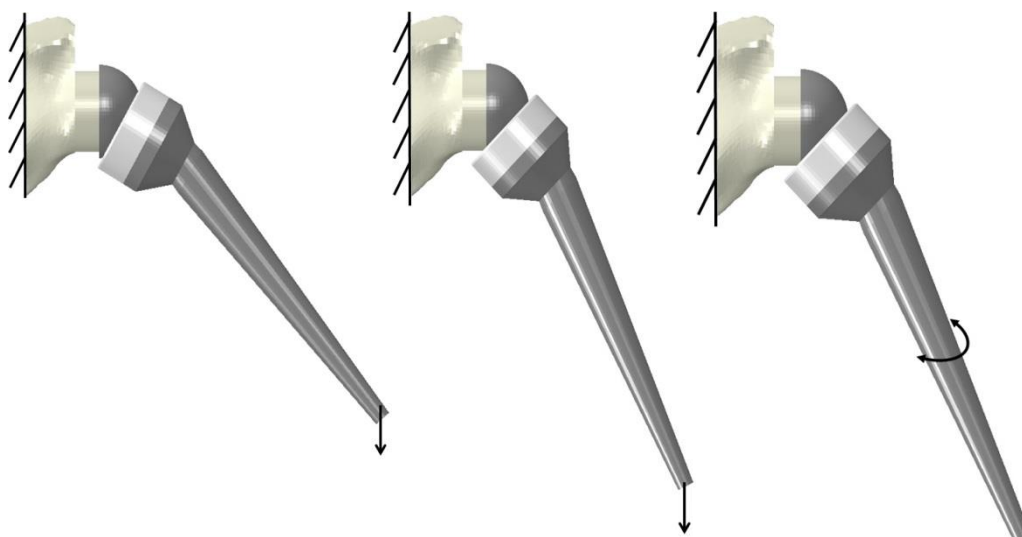
Figure 2-6 Schematic of loading conditions from left to right. The medial edge of the glenoid is fixed. A load equivalent to the weight of the arm is placed on the distal end of the stem. The humeral component is allowed to adduct until impingement with a fixed center of rotation at the center of the glenosphere. Once impingement occurs, the humeral component is fixed in impingement, and the humeral component undergoes an internal/external rotation arc.

Results

Range of Motion Analysis

In the first defined experiment studying range of motion, the model predicted impingement for a medialized implantation (represented in this experiment with a 10 degree inferior tilt) at 25° of abduction. However, the lateralized model (represented in this experiment with an 8 mm BIO cylinder) was impingement-free at 25° of abduction, and the lateralized model was able to adduct to 3° before impingement occurred.
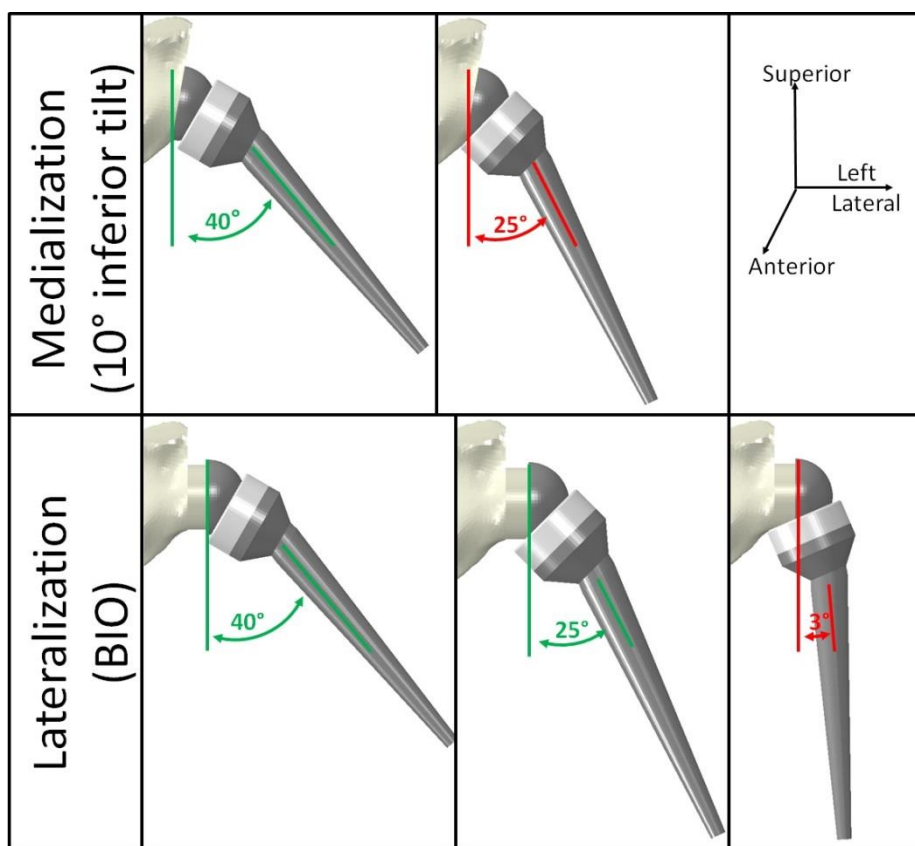
Figure 2-7 Results of the range of motion runs for the medialized and lateralized models. The lateralized model has practically no adduction deficit (3°) while the medialized model impinged at 25°.

Stress Analysis

For the medialized model, the maximum contact stress was 710 MPa at 25° of adduction. For the lateralized model, the maximum contact stress was 729 MPa at 3° of adduction. The contact stress patches are shown below. For both models, peak stress was seen when the humeral component and glenoid surface were co planar. At this time, the impingement and polyethylene strains were greatest. Overall, the stress values and contact patches are similar at impingement.
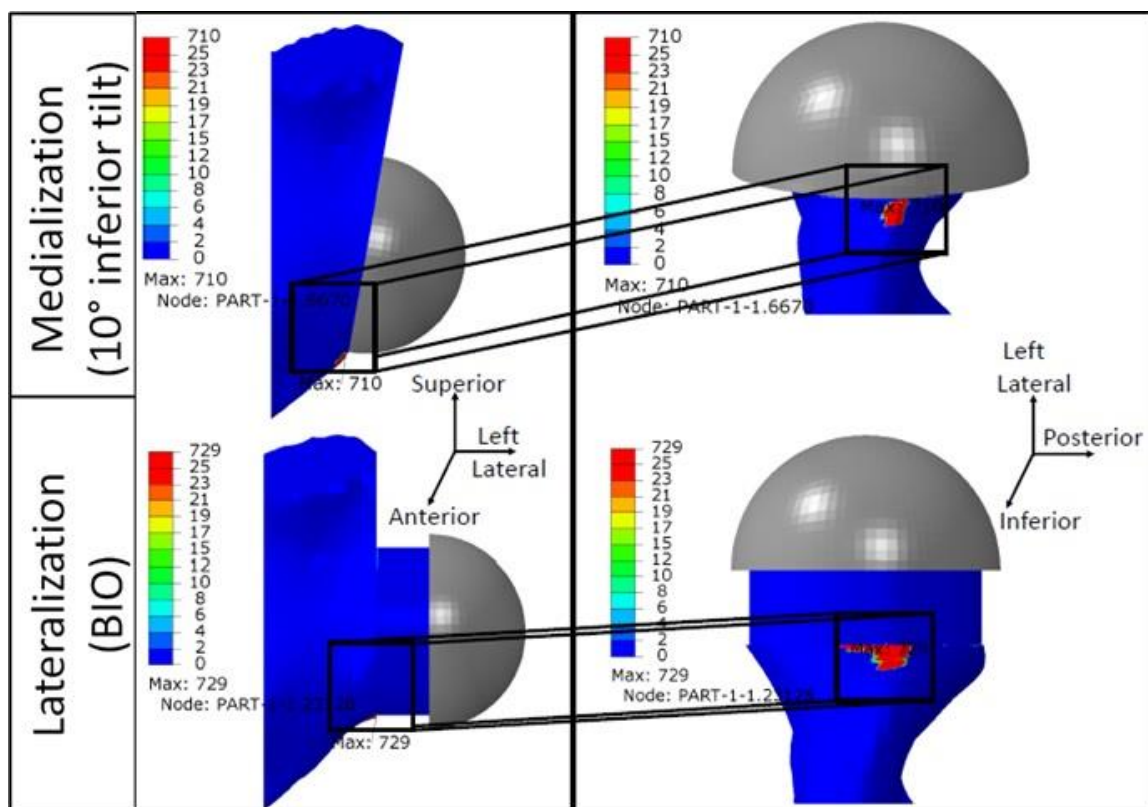
Figure 2-8 Contact stress seen in the inferior region of the glenoid. The stresses are scaled from 0-25 MPa. The number above the upper limit of the scale is the maximum values. All stress values 25 MPa or higher are represented in red. Comparable stress and contact patches are seen in both the medialized and lateralized models.

Discussion

Range of Motion Analysis

The adduction deficit values calculated correspond well with literature values. In our model, lateralization was able to increase the adduction range of motion by over 20°. In Boileau et al. 2011, it was found that lateralization with a BIO cylinder was effective at reducing adduction deficit [33]. Also, Gutierrez et al. 2008 found that lateralization was the single most effective way to increase range of motion in RSA, more effective than glenosphere position and tilt [60].

Stress Analysis

The stress values computed by the model were deemed too high to be realistic. First, the yield strength and ultimate strength of UHMWPE is reported to be 21 and 48 MPa respectively [68]. In other words, the polyethylene cup would yield and fail before these stress values would be seen. The unduly inflated stress values can be attributed to the fixture of the center of rotation, as well as the inability of the humeral component to abduct out of impingement during the internal/external rotation motion. In reality, the center of rotation would not be fixed to be the center of the glenosphere. In addition, the humerus would be able to lift off, translate, and adjust to the large load being placed on it, effectively moving the center of rotation

For future studies, the boundary conditions of the humerus were changed to reflect these lessons learned. However, these preliminary models provided proof of concept. Finite element models can be used to calculate range of motion for different implantations. In addition, complex contact between the humeral component and inferior ridge of the glenoid can be computed. Finally, many areas needing additional effort were recognized, including loading conditions.

CHAPTER 3

MODEL REFINEMENTS TO STUDY EFFECTS OF

LATERALIZATION ON IMPINGEMENT-FREE RANGE OF MOTION

AND DELTOID FORCE REQUIREMENTS

Model Advancement Goals

In the original model, boundary conditions of the humerus did not adequately represent in-vivo conditions. A static center of rotation for the humerus was defined at the center of the glenosphere. In an effort to better represent the in-vivo situation, the model complexity was increased to accommodate more natural loading. This involved first relaxing humeral motion so that it was not required to rotate strictly about the center of curvature for the glenosphere. Next, to better capture deltoid muscle force actuation, a series of elements were introduced to model the deltoid muscle. Additionally, elements of the proximal humerus bone were added to include their interaction with the deltoid muscle line of action.

Model Development

Humeral Geometry

A segmented humeral surface was generated from the Visible Female CT images using a similar methodology to that used for definition of the scapular geometry. The humeral bone surface and a surface model of the humeral implant were imported into Geomagic Studio, and the bone model was manually fit to the humeral implant model. The humeral long axis was fit to the stem. In addition, the humeral cup was best fit to the humeral head to replicate surgical technique. The modeled implantation was confirmed as being reasonable and reflective of implantations obtained clinically.
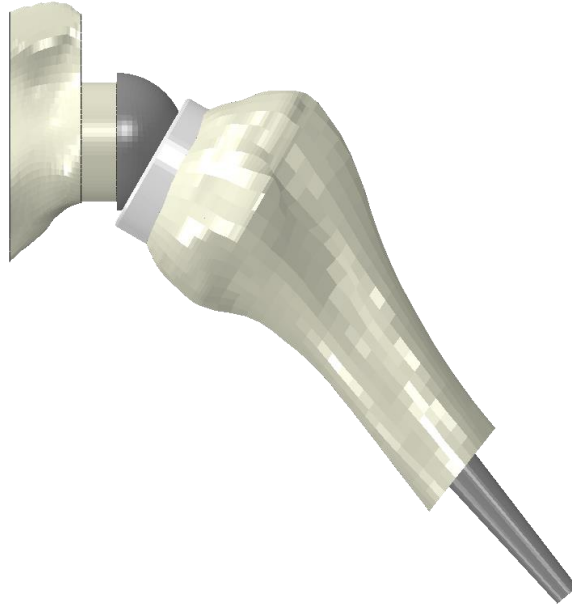
Figure 3-1 Model with completed humeral mesh. The geometry was obtained from segmented CT images of the Visible Female, and the mesh was generated in TrueGrid. Due to the high mesh refinement in glenoid area, element boundaries were removed for clarity.

Lateralization Model Generation

In the literature review, several different implantation techniques and types were discussed. From the exhaustive research surveyed, no single conclusive optimal implantation was determined. One variable studied currently is implant lateralization, with many surgical techniques promoting lateralization of the glenosphere by 5 or 10 mm. To better understand the effect that lateralization has on range of motion as well as muscle mechanical advantage, several models of varying lateralization were created in TrueGrid. Models with 2.5, 5, 7.5, 10, 12.5, 15, and 20 mm of lateralization by BIO were created as well as a medialized model with 10° of inferior tilt.

10° Tilt 2.5 mm BIO 5 mm BIO 7.5 mm BIO

10 mm BIO 15 mm BIO 20 mm BIO
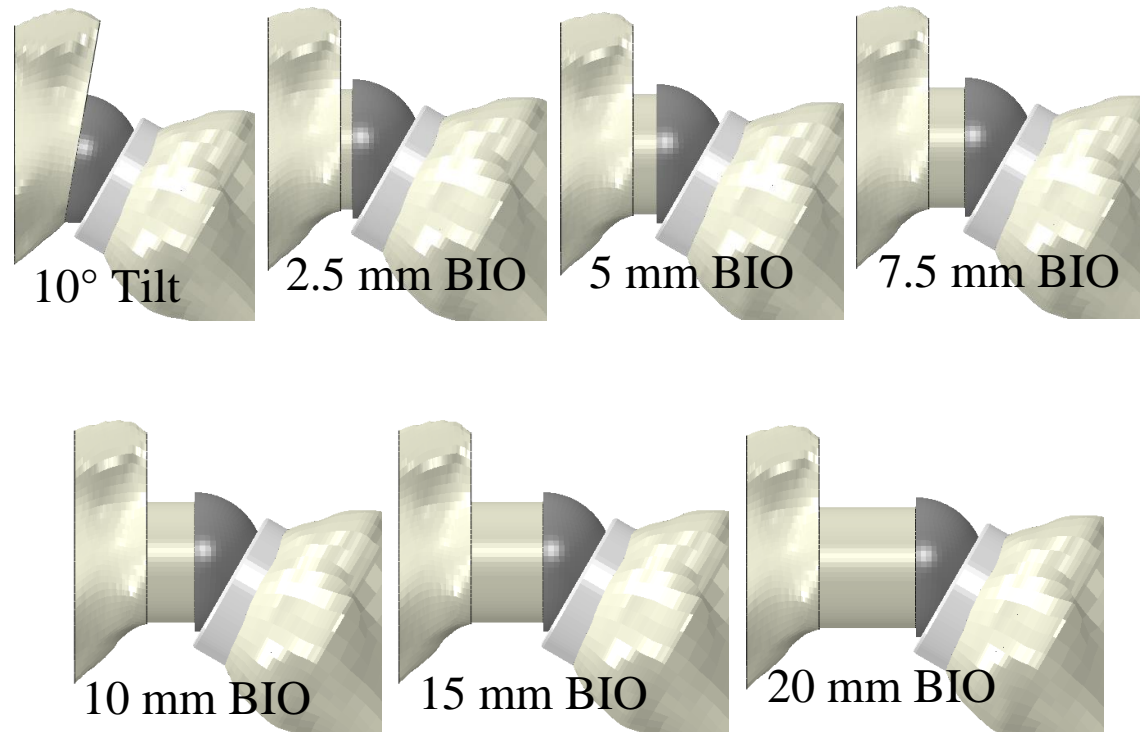
Figure 3-2 Frontal view of the seven models tested. The first model is medialized by 10° inferior tilt. The remaining models are lateralized by BIO.

Connector and Slipring Elements

Abaqus includes several special-purpose elements that were considered for use in modeling joint capsule restraints and deltoid muscle action. Connector elements are used to model kinematic or kinetic couplings between distinct finite element entities. Simple connector elements include springs. However, more complex connector elements can be used to restrict or create motion in many degrees of freedom.

Slipring elements are a specific type of connector element defined for use in Abaqus. They are used to model material flow as well as stretching between two points of a belt system. They are particularly useful for modeling cable and pulley systems. One slipring element consists of two nodes acting as pulleys, and the connection between the nodes acting as the cable. The slipring elements can be connected in series to represent a complete cable system. The flow rate of the cable can be varied at every node (pulley), and the nodes can be tied to the position of rigid bodies.

There are several potential uses for slipring elements in the current model. One use is in the definition of a nonlinear spring to model the complex material properties of capsular soft tissues. Abaqus/Explicit prefers the use of connector elements as opposed to spring elements in cases where displacement of both ends is desired. By defining that no flow occurs at the ends of one slipring element, a spring element is essentially created. These de-facto spring elements can be defined with many material properties including force-displacement data for creating nonlinear elastic elements, as well as damping coefficients to create viscoelastic elements. Because of this, the slipring element can be used as basic springs, or these complex properties can be applied to series of elements modeling soft tissue.

In addition, these slipring connector elements can be used to model muscles as a cable threaded through a series of nodes. The lines of action of the muscle can change with the position of the humeral component/humerus if the nodes are tied to the humeral

rigid body. By pulling on one end of the cable using either displacement or load control, humeral motion can be generated.

For example, if a series of slipring connector elements were defined originating at the acromion, wrapping around the humeral head, and connecting to the insertion site of the deltoid, a simplified muscle could be defined. A force or displacement could be applied to the proximal end of the slipring element, and the resulting force would wrap around the humeral head and pull on the distal end of the slipring element. The result would be motion of the humerus similar to that of a deltoid muscle contraction if the slipring position is defined to coincide with the line of action of the deltoid muscle.

Figure 28.1.5–29 Connection type SLIPRING.
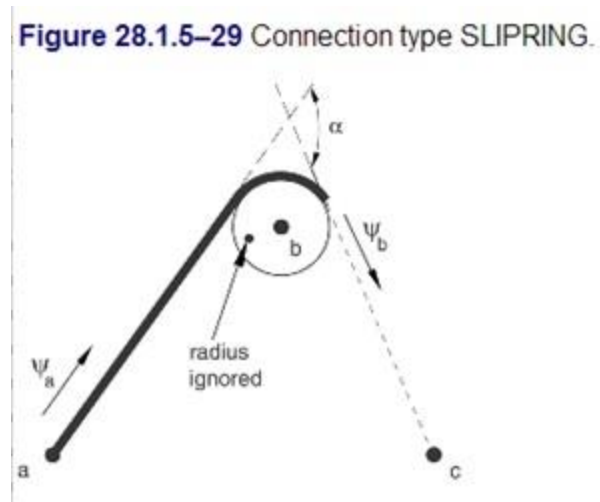
Figure 3-3 Diagram of slipring connector element definition. In this diagram, a slipring connector element has been defined between nodes a and b. The slipring element is designed to replicate a cable and pulley system in a simplified manner. The element connecting nodes a and b represents the cable, and the nodes represent the pulley. The nodes can be tied to rigid body definitions in order to apply displacement to the rigid body itself. In this way, displacement and forces can be applied to the rigid body through the slipring connector elements. Taken from Abaqus 6.12 documentation [71].

Humeral Constraint

In the models described in the previous chapter, the humeral center of rotation was fixed to the center of the glenosphere. Although this boundary condition works well when the humeral cup is able to fully conform to the glenosphere during the middle region of the range of motion, a fixed center of rotation is not meaningful when impingement occurs. A static center of rotation precludes the modeling of dislocation caused by impingement and does not reflect the true biomechanics of the shoulder. In vivo, joint laxity is often present. As discussed earlier, multiple soft tissue structures provide stability in the healthy anatomic joint. However, RSA patients by definition have debilitated rotator cuffs, and oftentimes entire muscle groups, such as the supraspinatus have deteriorated to non-functional levels [57]. While RSA geometry provides stability, joint laxity is still present due to the diseased nature of the musculature.

However, the ligamentous structures of the joint capsule are oftentimes still intact or are repaired while closing the wound. To better simulate the anatomic condition, four axial connector elements were introduced with the properties of the middle glenohumeral ligament of the joint capsule, calculated using ligament stress-strain data and average ligament cross-sectional area [2, 3, 72]. Axial connector elements are connector elements defined in Abaqus documentation. These elements create a connection between two nodes similar to spring elements. However, axial elements can be defined with tabular nonlinear spring stiffness values as well as tabular nonlinear damping values. In addition, Abaqus/Explicit requires axial connector elements in the place of spring elements in models were neither end of the element are fixed. The glenoid ends of the axial connector elements were prescribed initial pre-stress displacements, and were then fixed. The humeral ends of the axial connector elements were tied to the humeral rigid body. This provided an approximation of the joint capsule without requiring in-depth material and geometry models. For uses of obtained range of motion and calculating deltoid muscle forces, these boundary conditions were deemed satisfactory. This simulated ligamentous

support provided the necessary stability to hold the humeral component against the glenosphere during normal articulation without artificially constraining the humeral cup to remain on the glenosphere at the extremes of motion.

Loading Conditions

Deltoid Muscle Definition

On this project, early attempts to model the deltoid included modeling spring elements. However, spring elements were found to be ineffective in modeling the complex wrapping of the deltoid and in providing the precise control needed to produce motion. Slipring elements can be defined with the same or more specific material properties as classical spring element, while also possessing the ability to model wrapping and contribute to rigid body motion. The deltoid muscle was modeled using one series of slipring elements. The deltoid contains three major sections or heads that together generate the bulk of abduction force. In this study, the deltoid muscle was modeled as one body, because the deltoid muscles work together with similar lines of action to achieve abduction motion. The position of the deltoid slipring elements were defined to lie in the coronal plane in order to create pure coronal plane motion. The position of the slipring elements was based from anatomy, with the origin of the elements corresponding to the position of the acromion, the middle section of the slipring element complex wrapping around the humeral head, and the distal portion of the slipring element complex corresponding to the insertion of the deltoid.
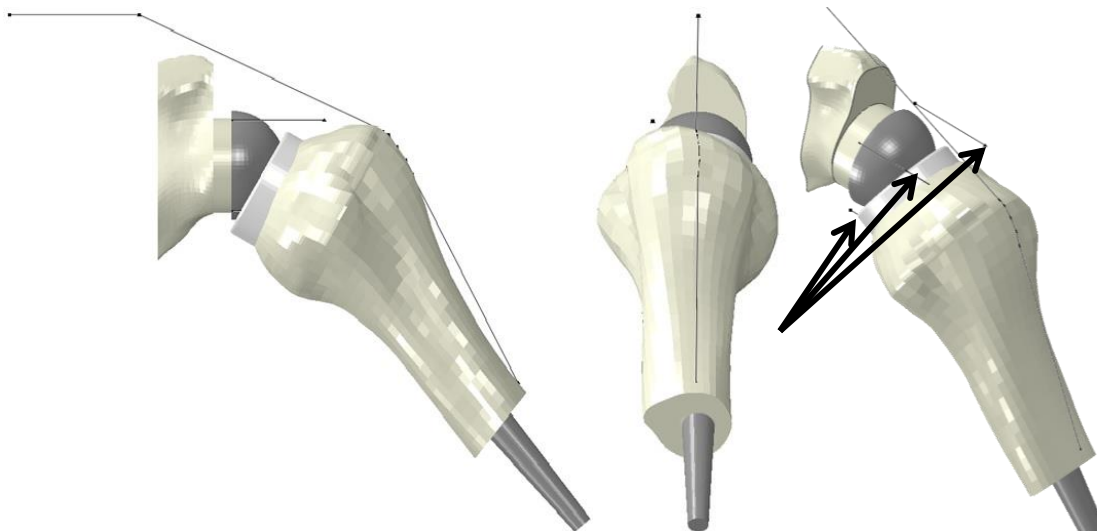
Figure 3-4 Anterior (left), lateral (center), and oblique (right) views of the 5 mm BIO model. Four slipring elements are used to provide stability for the humerus, and one series of slipring elements is used to model the deltoid muscle forces in the frontal plane. The slipring elements are difficult to observe in normal anatomic views, but the oblique view displays three of the four slipring elements used to model the capsule, indicated by the black arrows.

Test Protocol

Range of Motion Test

In all models, the humeral component started at 40° of abduction. The first run tested adduction deficit by allowing the humeral component to adduct freely under the weight of the arm, defined in the previous section, until impingement of the humeral cup on the scapula occurred. The angular displacement of the humeral implant at the time of impingement was found.
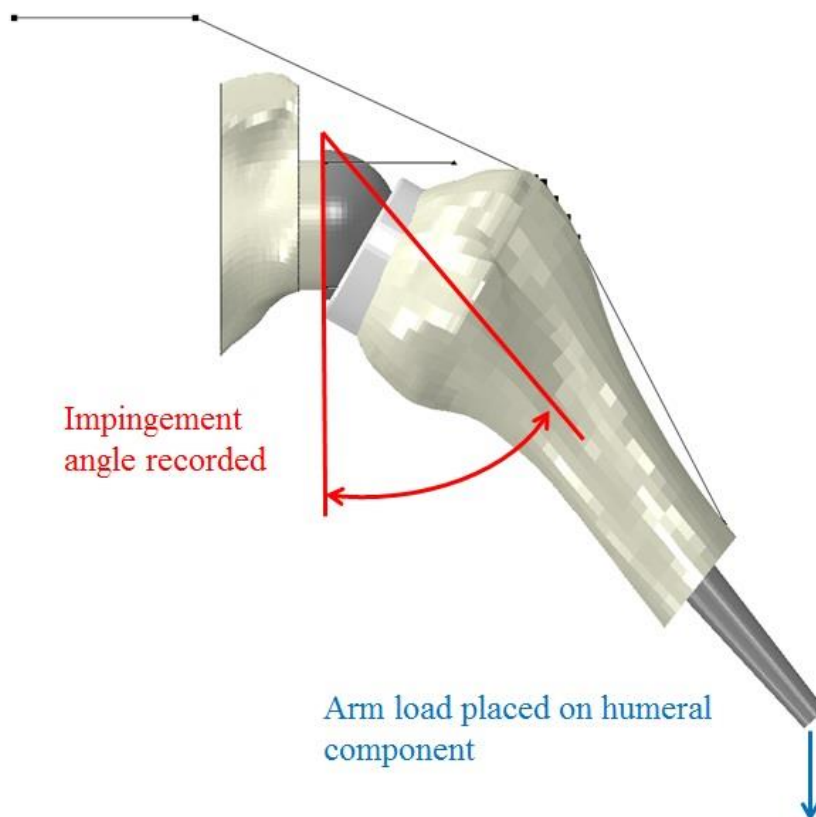
Figure 3-5 Impingement test of implantation. The humeral component starts in 40° of frontal plane abduction. A load is placed on the stem, and the humerus is allowed to fall until impingement, and the impingement angle is then recorded.

Muscle Force Test

In the second run, an adduction moment was applied to the humeral component, and the superior end of the slip ring element complex was held. The moment value was computed from clinical testing data. In the clinic, shoulder strength data were collected from patients post-operatively following RSA. Internal rotation, external rotation, and scapular plane elevation was tested using a microFET2 dynamometer (Hoggan Health Industries, Salt Lake City, Utah). To assess scapular plane elevation strength, the patients were seated and asked to place their arm in a handshake position. The clinical assistant then asked the patient to elevate the arm while simultaneously restraining it with the

dynamometer (Figure 3-6). The peak force was recorded over three trials. For control

purposes and to test rehabilitation of the joint, the non-operative shoulder was tested as

well. Force data from a 62 year old female patient was obtained and using average female

upper limb data, an equivalent moment of 21114 Nmm was calculated [70].

Figure 3-6 Image of the author replicating shoulder strength test. The subject is asked to
provide peak scapular plane abduction forces, and the clinical assistant
restricts motion of the patient with the dynamometer for 3 trials of 5 seconds.
The peak force of each trial is recorded.

This calculated moment was applied to the humerus as an adduction moment.

When reaction forces in the cables oscillated less than 10 N, steady state was assumed,

and cable reaction forces was recorded. The results provide the tension required by the

cable to counteract the applied adduction moment and restrict humeral motion. More

importantly, this model acts as a free-body diagram to calculate the deltoid force required

to resist the moment caused by the external force of the fixed dynamometer.
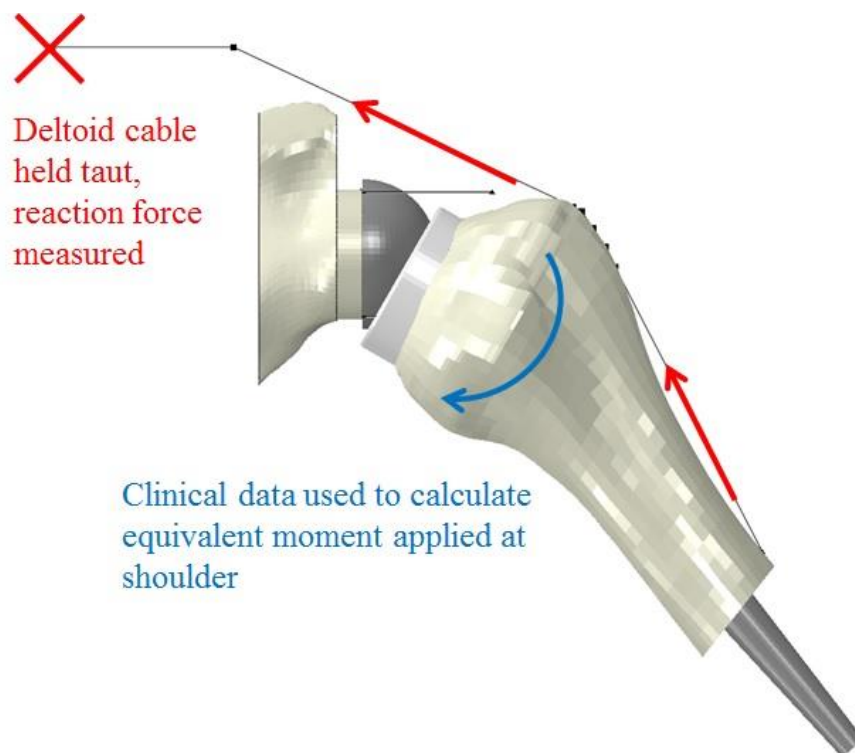
Figure 3-7 Muscle force test loading conditions. For this test, the deltoid cable is held taut and an external adduction moment is applied to the humeral component. The reaction force of the end of the deltoid cable is recorded.

Results

Abduction Angle

Impingement angle was found to decrease with increasing lateralization. For the model with no lateral offset (the model with a $10°$ inferior tilt glenoid cut), the humerus impinged at $25°$ of adduction. The impingement angle decreased with every increase in lateral offset. Models with 10 mm of lateralization or more predicted negative impingement angles, signifying that the humerus would need to adduct past anatomic position to produce impingement. For example, the most lateralized model (the 20 mm BIO) impinged at $-3.65°$ of adduction.

Deltoid Force

While impingement angle decreased with increasing lateralization, the muscle
force required increased with increasing lateralization. The medialized model registered
1133 N of force, and the most lateralized model registered 1483 N of force, an increase of
30.9%. A linear relationship was seen for the deltoid force required.

Mechanical Tradeoffs
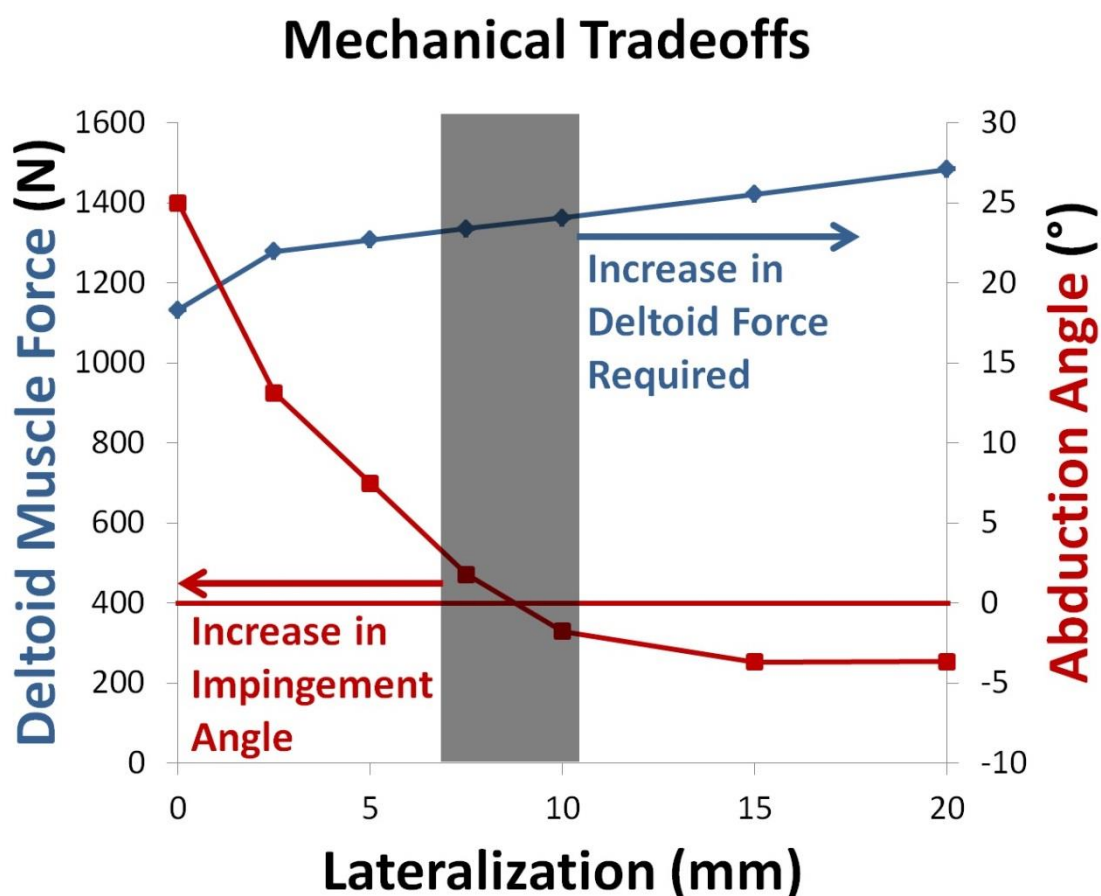
Figure 3-8 Results of impingement and muscle force tests. Increases in lateralization
decrease the angle of impingement while also increasing the deltoid muscle
force required to resist an applied abduction load. The grey box represents the
amount of lateralization most often used in current implantations.

Discussion

The model computed muscle forces that are well within the range of reported values; Garner and Pandy found the maximum deltoid force available for healthy young individuals is 2000 N [73]. Comparing the deltoid load data computed with that study, it seems reasonable that older patients would be capable of generating the muscle forces seen in the model. Control data gathered in the clinic agrees with this hypothesis. It was found that in the shoulders of patients with RSA, the deltoid was able to generate just over half the load recorded in the healthy contralateral joint 6 months post-operation and 90% load 12 months post-operation. In addition, recent literature indicated that no statistical declines in shoulder strength occur for males and females in an aging work population [74]. Other research has shown isokinetic and endurance strength of the shoulder muscles remain fairly constant from age 19 to 59 [75].

The results from the impingement and muscle tests correlate very well with conventional statics and dynamics concepts. When the center of rotation was lateralized, the deltoid muscle force required to abduct the arm increased. This makes sense since the applied moment remains constant, but the moment arm of the deltoid cable force decreases. In order to counter balance the decrease in moment arm length, an increase in muscle force is required.

However, to decrease the muscle force required to achieve abduction, medialization is required, producing an increased adduction deficit. Therefore, deltoid muscle strength must be balanced against impingement angle when deciding to medialize or lateralize the RSA hardware, and there is not a simple one-size-fits-all approach. For example, a heavier patient may achieve natural impingement between their elbow and thoracic cavity before impingement between the humeral cup and the scapula. For these large patients, less lateralization is required to prevent impingement, allowing the surgeon to implant with less offset and provide more deltoid leverage to the patient. However, for patients with less adipose tissue around the upper limb and thoracic region,

more lateralization is required to prevent impingement between the humeral cup and the glenoid. In general, surgical technique should be guided by the knowledge that changes in center of rotation not only affect adduction deficit but muscle mechanical advantage.

CHAPTER 4

APPROACHING ANATOMIC REALISTIC MODELING

OF DELTOID FORCE GENERATION

Model Development Tools and Techniques

Implementing an Inverse Dynamics Approach

In order to provide more realistic muscle force approximations, an inverse dynamics model of the RSA was developed to complement the existing FE model. Using inverse dynamics software, muscle forces and joint moments can be estimated from known motions of rigid bodies. These muscle loads can be used by themselves to increase understanding of the joint studied, or they can be integrated into a finite element model.

For this project, SIMM and OpenSim software packages were utilized in tandem. In SIMM and OpenSim, muscles are discrete elements defined with Hill-type muscle behaviors, parameterized by optimal fiber length, peak force, tendon slack length, and pennation angle. Additionally, these muscle elements contain wrapping capabilities to interact with bone surfaces. Motions can be defined for the segment models such as elevation and rotation, and the muscle points are defined with connection to the rigid body motion of the segment.

SIMM was one of the first commercially available inverse dynamics software packages for biomechanical application. Advantages include uncomplicated coding language for model generation, a robust graphical user interface, and the ease of muscle, joint, and bone model positioning. However, compared with OpenSim, SIMM is expensive and provides limited motion generation functionality. Because of this reason, this project utilized OpenSim as the primary inverse dynamics solver. OpenSim is based upon SIMM, but contains more functionality and capabilities built in to incorporate motion tracking data. As opposed to SIMM, OpenSim is free, open source software

available online at https://simtk.org/home/opensim. Also, OpenSim is available with free online support and open source, literature-reviewed models of many joints. For these reasons, OpenSim was chosen as the preferred inverse dynamics simulation software for this project.

This project utilized SIMM and OpenSim in a similar fashion to the relationship between TrueGrid and Abaqus. SIMM was used strictly as a preprocessor to create musculoskeletal inverse dynamics models. The SIMM model can also calculate isometric muscle forces, muscle moments, and muscle moment arms for any point in given motion. To compute inverse dynamics solutions, a SIMM model can be exported to OpenSim. Using a muscle force optimization algorithm, OpenSim can calculate muscle forces for a given limb motion. These motions can be defined manually by the user, such as a simple abduction movement, or motion tracking data from a patient can be imported to define a more realistic motion profile.

<u>SIMM Shoulder Model</u>

While the majority of inverse dynamics modeling has focused on the lower limb and gait-related activities, an identical modeling approach can be used in the upper extremity. Fewer inverse dynamics models exist due to the increasing complexity that occurs with the increase in the number of joints and mobility of the joints found in the upper limb. This project utilized the Stanford VA Upper Limb model, accessible via the OpenSim support site, which contains the thoracic cavity and all the bones of one upper limb. The shoulder, elbow, forearm, wrist, thumb, and index finger joints are defined and can be controlled via 15 degrees of freedom. In addition, 50 muscles are defined with proper wrapping surfaces and bone associations. Complete model description can be found in Holzbaur et al. 2005 [76]. The Stanford VA Upper Limb model was also used as the basis for creating a modified finite element model. The OpenSim model fully defined

three-dimensional upper limb geometry, was validated to experimental data, and, as mentioned earlier, is provided freely by the authors to conduct additional research.

FE Model Geometry Adjustment

For all previous models discussed in Chapters 2 and 3, the position of the humerus and scapula were idealized so the scapula and humerus were roughly in the same plane, effectively creating two-dimensional loading conditions. In the actual shoulder, the scapula is positioned at an angle relative to the humerus due to the shape of the thoracic cavity on which the scapula lies. The medial aspect of the scapula tip is posterior with respect to the lateral aspect.

The existing FE model was aligned with the validated anatomic position of the bones used in the SIMM model so that the position of the humeral and scapular meshes more accurately replicated the native geometry. This was done by exporting the surface models used for TrueGrid meshing and the bone surface models defined in SIMM to Geomagic Studio. The TrueGrid meshing surfaces were aligned to the SIMM surfaces using an iterative closest point algorithm available in Geomagic Studio. Deviation maps of the agreement between the FE mesh and the SIMM bones surfaces were generated. The greatest deviation of 8 mm for the scapula was measured in the wing region, a section of the scapula not included in the glenoid finite element model. For the glenoid region, maximum deviation was 2 mm. Because the glenoid region is the only portion of the scapula meshed and the largest deviation values were far from the impingement site, this error was deemed acceptable. For the humerus, deviations from the SIMM surface were sub-millimeter. The rigid transformation calculated by the iterative closest point algorithm was incorporated into TrueGrid to orient the FE mesh in SIMM-based anatomic position.

After realignment, the new scapular and humeral meshes were exported to Geomagic again to verify the transformed mesh positions. In the previous alignment

procedure, Visible Female native bone geometry was fitted to the SIMM native bone

geometry positioned in the SIMM native shoulder configurations. However, rigidly

transformed meshes were repositioned with slight overlap of the humerus and scapular

mesh, due to the change in center of rotation between native and RSA shoulder. Because

of this, the humeral meshes needed to be adjusted. Spheres were fit to the glenosphere

and the humeral cup in Geomagic, and new transformations to align the two spheres were

created and implemented in TrueGrid to create accurate model positions.
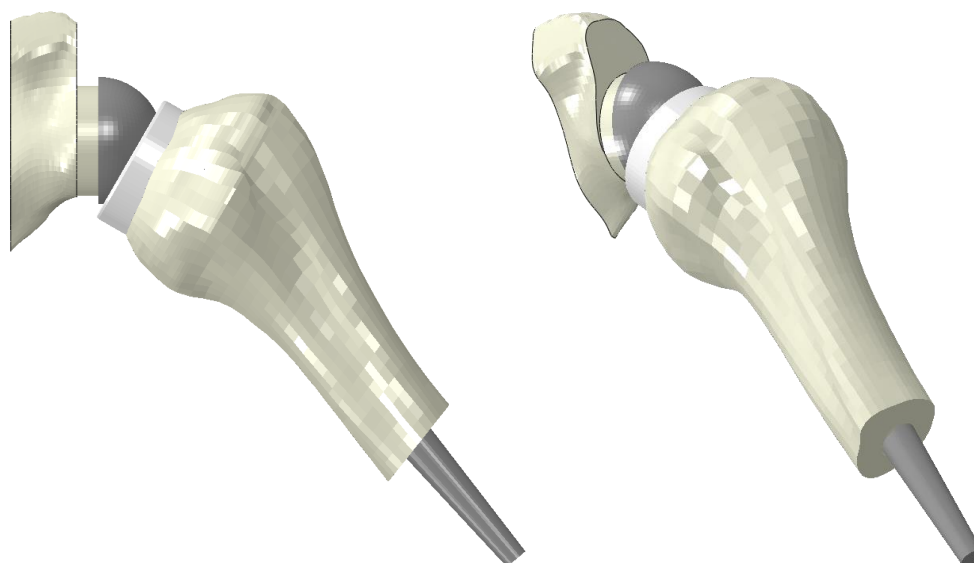
Figure 4-1 Anterior views of the original (left) and anatomically adjusted (right) RSA
models. The orientation of the anatomic model was achieved by rigidly
transforming the FE mesh to the position of the SIMM shoulder model bony
geometry and applied small translations to adjust for different centers of
rotation. In the anatomic model shown, the humerus was positioned in the
scapular plane. In the clinical test protocol, the scapular plane is defined as
45° anterior from the frontal plane, and the same definition was used in the
model.

SIMM Model Adjustment

In addition to adjusting the position of the FE model to a more anatomic

configuration, the bone geometries of the SIMM model were adjusted to represent RSA

geometry instead of native geometry. The FE scapular and humeral mesh geometries were exported from Abaqus/CAE into .obj surface files, and the surface files were imported into the SIMM model. The center of rotation of the glenohumeral joint with the RSA hardware included was adjusted to reflect the change in center of rotation. From the native shoulder to the RSA shoulder, the center of rotation translated 40 mm anteriorly, 6 mm inferiorly, and 22 mm medially.
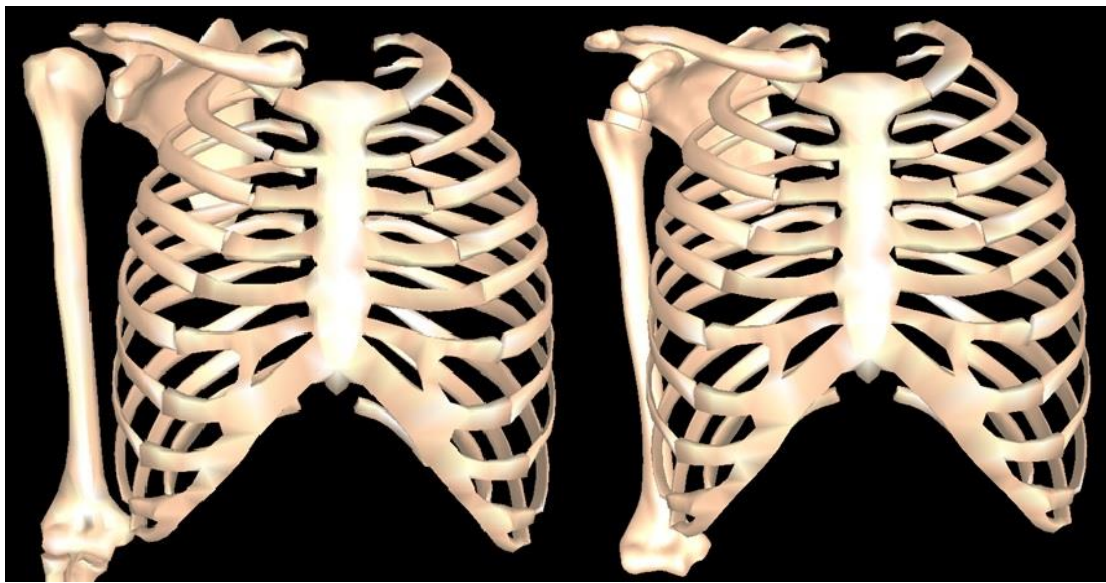
Figure 4-2 Anterior view of the Stanford VA Upper Limb Model (left) and modified RSA (right) OpenSim models. The original native VA Upper Limb Model is comprised of an entire upper limb with movement at the elbow, forearm, wrist, index digit, and index digit joints. The modified RSA model has all joints distal to the glenohumeral articulation removed, and, in addition to changing bone geometry, the joint center was relocated to the center of the glenosphere.

Loading Conditions

Scapular Motion

As described in Chapter 1, not all rotation of the shoulder occurs at the glenohumeral joint. A large portion of shoulder rotation occurs at the scapulothoracic

joint, and impingement angle calculations may be inaccurate if only glenohumeral motion is modeled. In order to better predict impingement angles, scapular rotation was added to the model.

The first step in implementing scapular motion was to determine the impingement angle of different hardware implantation positions with no scapular rotation taken into account. This preliminary set of FE jobs was nearly identical to the impingement angle tests in Chapter 3; the only change was the difference in mesh positioning. After computing impingement angles, the SIMM model was used to determine the scapular position corresponding to the computed impingement angles. Discussed earlier, the translation and rotation of the humerus is dependent on the position and rotation of the scapula. In the SIMM model, scapulo-humeral rhythm had been defined. Thus scapular position for a given abduction angle could be determined in SIMM.

The SIMM model was placed in an abduction angle equal to the impingement angle computed in the static scapula case, and the scapular bone surface was exported to Geomagic Studio. These surfaces reflect the scapular bone position for a corresponding abduction angle. All scapular surfaces were fit to the 0° abduction scapula using the iterative closest point algorithm in Geomagic Studio, and the rigid body transformations were recorded. These values were used to create a scapular rotation profile including the precise x, y, and z rotations the scapula undergoes from 40° to 0° of abduction, as modeled in SIMM. Translations were calculated to be in the sub-millimeter range and were deemed to be negligible.

A sheet of elements was added to the medial side of the glenoid mesh, defined as rigid, and used as a control surface to prescribe scapular rotation. Using the scapular rotation profile, scapular rotations were prescribed using the reference node of the rigid surface. The scapula started in the position corresponding to 40° of scapular plane abduction and rotated to the positions corresponding to 0° of scapular plane abduction.

By including the scapulothoracic motion, a more accurate range of motion dataset could be calculated.

<u>Humeral Stability and Deltoid Cables</u>

In Chapter 3, slipring elements spanning the glenohumeral joint were introduced to maintain stability of the articulation during motion and to facilitate deltoid muscle modeling. The anatomically aligned FE models contained similar element sets to create stability and measure deltoid muscle force. In the previous chapter, four axial connector elements were incorporated into the model to create stability in the joint. However, stability was along the superior/inferior axis was created from the deltoid muscle slipring element definition. For this reason, only two axial connector elements were introduced in this model to provide stability about superior/inferior axial.

Two additional axial connector elements were introduced to resist rotation of the humerus out of the scapular plane. The axial connector elements were defined with double the stiffness properties as the previous capsule-approximating ligaments. In the clinical assessments, shoulder strength is evaluated in the scapular plane. To match that configuration, the elements defining the deltoid cable were adjusted to be positioned in the scapular plane. Also, in-vivo, the line of action of a muscle resides in the center of the muscle belly and not at the interface of the muscle and bone. To better replicate this, the cable representing the deltoid was moved above the humerus rather than wrapping around the humerus. The origin and insertion site of the slipring element series in the FE model was based on the origin and insertion site of the deltoid in the SIMM model, but adjustments were made to ensure the slipring elements were positioned in the same plane as the applied moment. These modifications to the FE model correlate with the muscle in the SIMM model where the deltoid resides above the humeral surface.
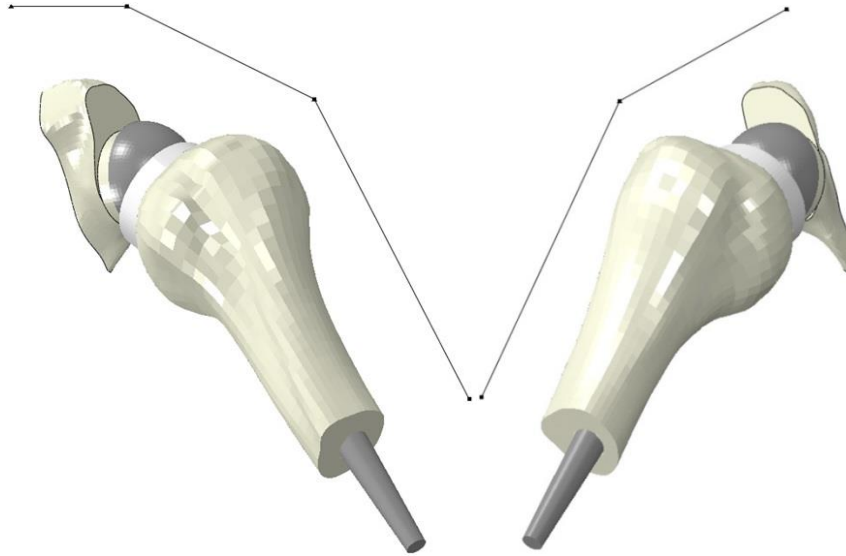
Figure 4-3 Anterior and lateral view of model after adjustment to the anatomic configuration. Two axial connector elements are used to provide stability for the humerus and humeral implant (not shown), and one series of slipring elements is used to model the sum of deltoid muscle forces in the scapular plane. The model displays the humeral component in the scapular plane.

Test Protocol

Range of Motion Test

Fixed Scapula

For these models, the range of motion tests from Chapter 3 were followed almost identically. The humerus was allowed to rotate downward until impingement occurred. There were two differences between the prior range of motion tests and these. In these models, the meshed geometries were repositioned to their anatomic positions as defined by SIMM. Two different sets of models were run to determine the difference in range of motion for frontal plane and scapular plane abduction. The humerus started in 40° of scapular plane abduction for the scapular plane tests, and the humerus started in 40° of frontal plane abduction for the frontal plane test.

Rotating Scapula

During previous range of motion tests, the scapula was fixed, and the humerus was the only bone allowed to rotate. In these anatomically oriented FE models, scapular rotation was prescribed using SIMM position data. The x, y, and z rotation values computed were applied to the scapula. The scapula rotated from its 40° abduction position to the 0° abduction position. In order to match humeral rotation to scapular rotation, the humeral motion was regulated using the deltoid cable. In pre-conditioning runs, a known velocity governed the end point of the cable, and the humeral rotation was recorded. These humeral rotations and deltoid cable velocities were used to determine the correct deltoid cable velocity to match humeral rotation to scapular rotation. For example, a velocity V was given to the end point of the cable. A humeral rotation of r was recorded. Since 40° of humeral rotation was desired, the new cable velocity would be $V*40/r$. Due to the numerically approximate nature of FE and element stiffness fluctuations inherent in Abaqus/Explicit, a few iterations were required to achieve 40° to within a few tenths of a degree.

Once adequate velocity and rotation values were empirically found, the models were run in a similar fashion to the range of motion test in Chapter 3. The impingement angles were computed by rotating the humerus until contact with the scapula was achieved, or the humerus reached 0° of scapular plane abduction.

Convergence Study Test

In order to determine the finite element mesh density required in this work, a convergence study was conducted. In TrueGrid, a 2.5 mm BIO lateralization model was created using four different mesh densities, containing 82,381, 156,753, 267,753, and 419,733 elements respectively. Each model was run through a scapular plan impingement test with a fixed scapula. The peak contact stress at the impingement site was recorded.
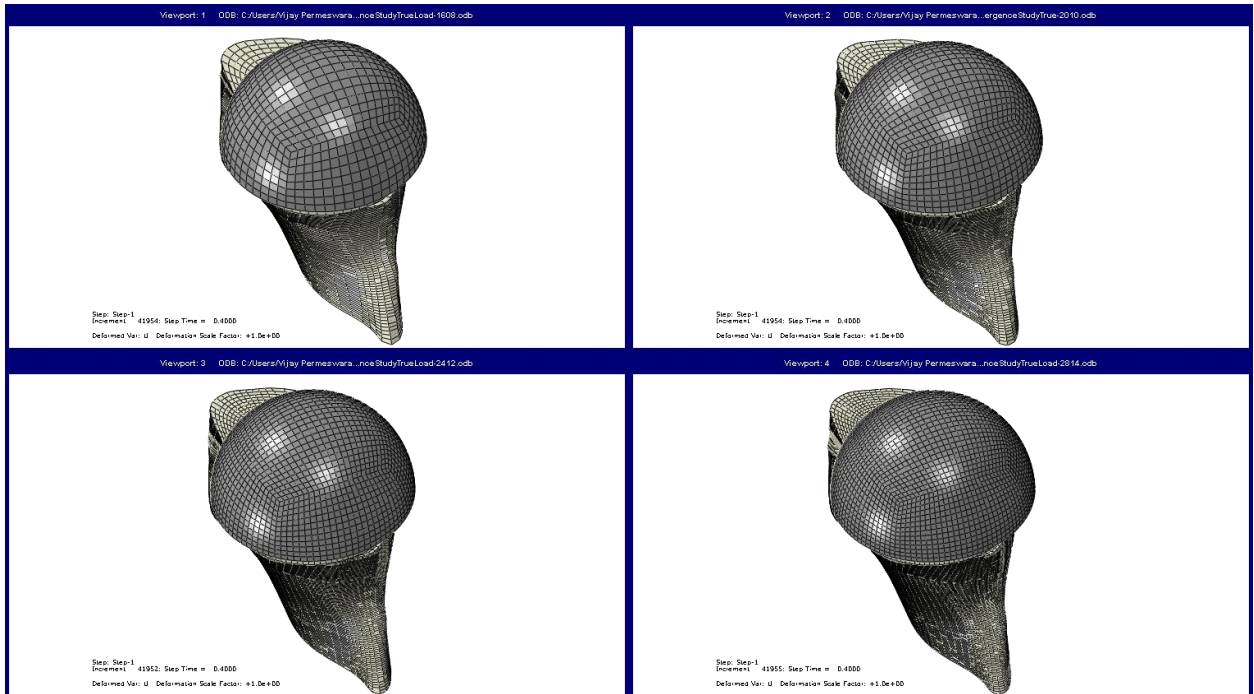
Figure 4-4 Image of four models created to study mesh density. The glenoid region of the mesh is shown. The mesh densities are 82,381 (top left), 156,753 (top right), 267,753(bottom left), and 419,733 elements (bottom right). While not shown, the humeral region was comparably meshed to correspond with each of the mesh densities studied.

<u>Muscle Force Test</u>

The muscle force test was carried out identically to the test protocol described in Chapter 3. An external moment equivalent to loads recorded clinically was placed on the humerus, the end of the deltoid muscle cable was held firm, and the reaction force at the end of the cable was recorded. Due to the static nature of this test, no scapular rotation occurs, and no scapular rotation modeling was required.

Results

Range of Motion Test

Fixed Scapula

A clear difference was seen between the impingement angle for the previous coronal plane and current anatomic models. The results presented in Chapter 3 for the coronal plane models indicated implantations with greater than 8 mm of lateralization had no impingement. However, the new anatomic model with adduction occurring in a frontal plane indicated impingement for all models, regardless of lateralization. In general, the impingement curve moved upwards, as evidenced when comparing the impingement curve in Figure 4-7 to the impingement curve in Figure 3-7. The medialized implantation impinged in the initial position of 40°. The 2.5 mm lateralized implantation impinged at 25.5°, the 5 mm lateralized implantation impinged at 17.7°, and the 7.5 mm lateralized implantation impinged at 9.1°. The highly lateralized models (10, 15, and 20 mm BIO) experienced impingement at the same angle of 4.5°.

The scapular plane abduction impingement curve was also found to be different than the frontal plane abduction impingement curve. The impingement angle for the medialized model was 21°, and the impingement angle for all models with 5 mm or greater lateralization was 8°. Overall, scapular plane abduction range of motion was less affected by lateralization.

Rotating Scapula

As expected, when scapular rotation was introduced to the model, impingement angles dropped sharply. For all lateralized models, no impingement between the humeral cup and the glenoid surface was detected. Impingement for the medialized model occurred at 8.4° of scapular plane abduction.

Convergence Study Test

The convergence study results calculated the same impingement angle for all mesh densities. The locations of contact computed were very similar for all models, as well. However, smaller contact areas and correspondingly much higher contact stress values were computed for the two highest mesh densities studied, compared to the two lowest mesh densities. The 267,753 and 419,733 element meshes calculated very similar stress values of 99.9 and 97.8 MPa, respectively.
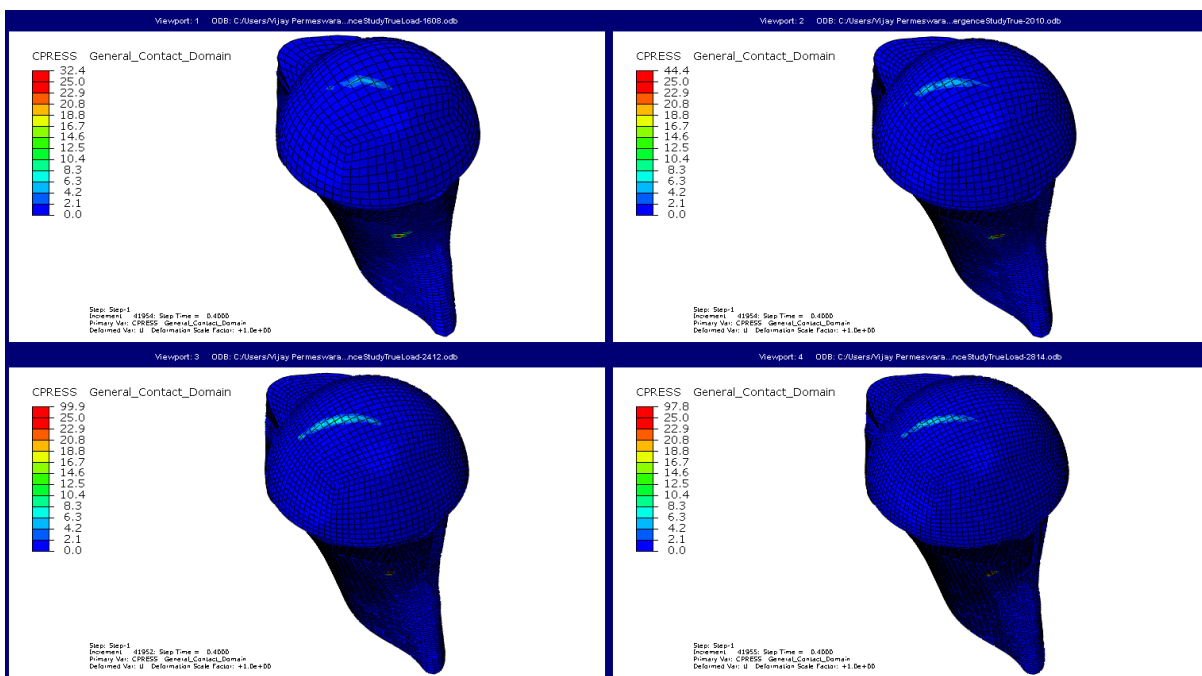
Figure 4-5 Contact pressure plots of four convergence study meshes. The areas of contact are similar between the different density meshes, with a region of humeral cup rim loading on the glenosphere and a small patch of contact highlighted by the red box where impingement occurred.
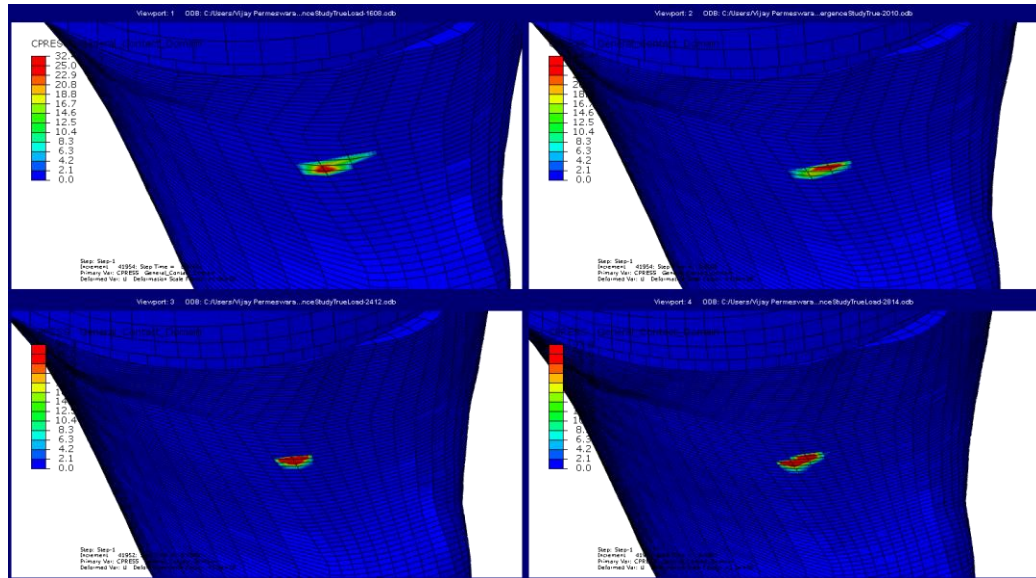
Figure 4-6 Close-up view of contact pressure plots at the impingement site. The region that contact occurs for all four models is very similar. In addition, maximum contact stress values at the impingement site for the two densest meshes are very similar (99.9 vs. 97.8 MPa).

Muscle Force Test

The deltoid muscle force required to abduct the arm in the scapular plane decreased in the anatomically oriented scapula models with respect to the previous coronal plane oriented models. For all implantation positions, the muscle force required was lower than the lowest value reported in Chapter 3. However the trend of higher required muscle forces with greater lateralization remained the same. As expected, the lowest deltoid force value (673 N) was seen in the medialized model. The force values required to abduct the arm in the scapular plane increased nearly linearly with increasing implant lateralization. A linear best fit to the force versus lateralization data ($R^2 = 0.98$) indicated that for every 1 mm of implant lateralization, an additional deltoid force of 8.4 N was required to abduct the arm in the scapular plane.
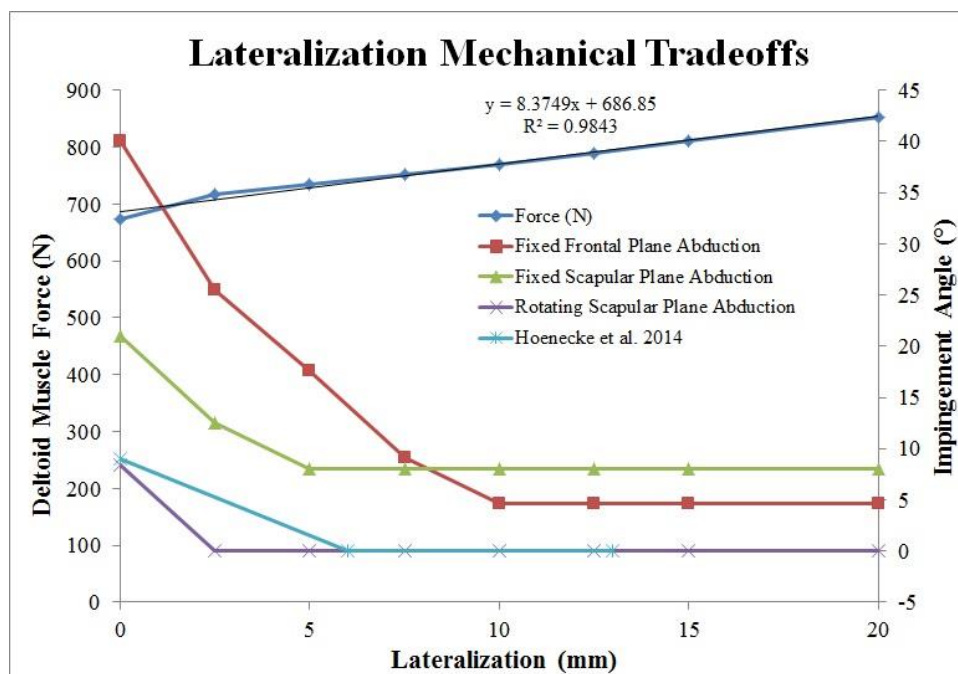
Figure 4-7 Results of the deltoid muscle force test and the range of motion test for the anatomically positioned models with fixed and with rotating scapula. Muscle forces were found to be much lower for the anatomic model versus the idealized mode. In addition, the impingement angle for a fixed scapula rose.

Discussion

Fixed Scapula Range of Motion Test

The work described in this Chapter indicates the importance of scapular and humeral orientation on the resulting biomechanical analysis of the shoulder. In the simplified coronal plane models used in Chapters 2 and 3, the humerus and scapula were in an almost two-dimensional relationship. That configuration omitted the subtle and important positioning of the bones in the joint. The anatomically oriented models introduced in this chapter incorporate the three-dimensionality of the joint. In prior models, the positions of the humerus and scapula did not reflect their true anatomic positions, where the scapula is tilted posteriorly with respect to the humeral position. In addition, the inferior edge of the scapula is tilted medially away from the humerus. These

changes have been made in the anatomic models and clearly influence the range of motion of the joint. In addition, it is clear that range of motion must be calculated for many motions in order to estimate the likelihood of impingement and scapular notching occurring. From the evidence presented here, the plane in which the range of motion is measured can change the angle of impingement by up to 20°.

Rotating Scapula Range of Motion Test

It is clear from the comparison of the fixed scapula and rotating scapula datasets that range of motion testing should not be conducted with a fixed scapula, or unrealistic results will be generated. Previous models reported in the literature and the models in Chapters 2 and 3 indicated that range of motion varies with implant positioning, often depicted with a gentle curve relating glenosphere position and range of motion [60, 77]. However, the results in Chapter 4 seem to suggest that a strong cut-off relationship may occur, where all implantations lateralized beyond a certain threshold do not impinge before 0° of adduction, and all implantations medialized to that threshold do impinge.
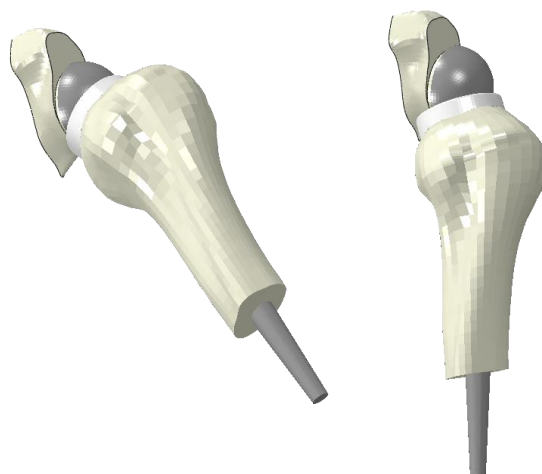
Figure 4-8 Image of 2.5 BIO before and after range of motion test. Appreciable scapular rotation occurs, affecting the physical position of the humerus, and changing the calculated impingement angle from 25° to less than 0°.

This current loading condition does not predict impingement. However, for many of the implantations, closer inspection revealed that impingement would occur within a few degrees. In addition, other motions, such as frontal plane abduction, are predicted to create impingement before 0°. Although the Chapter 4 results are accurate for the motion modeled, other motions need to be modeled to create a more encompassing indication of the range of motion each implantation is capable of providing.

Intuitively, these results are plausible. Anatomic data presented in Chapter 1 described a 1:2 scapulo-humeral rhythm. For the data above, it demonstrated that in the scapular plane, the rotating scapula models decreased the impingement angle by 12°. From the traditional 1:2 rhythm, the scapula would be expected to rotate 1/3 of the 40° the humerus traveled or 13.3°, a value close to the 12° seen in the data. In other words, the rotation of the scapula in this model contributed 12° to the range of motion in the medialized model, similar to traditional anatomic knowledge of scapulo-thoracic rhythm.
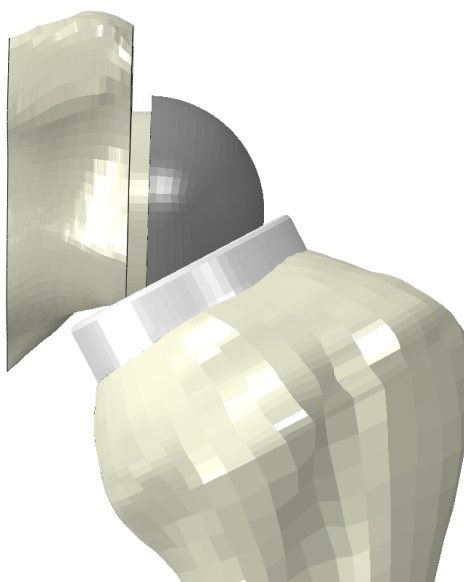
Figure 4-9 Close-up view of near impingement with 2.5 mm BIO model. Although no impingement occurred, slight external rotation of the humerus model would create impingement.

These results indicate the importance of incorporating scapular motion into a range of motion study. Without any scapular motion, prediction of scapular impingement is unreliable. Furthermore, it has been reported that CTA patients have increased scapular motion with respect to healthy shoulders [78]. In order to attempt to achieve shoulder function, CTA patients substitute pain-free scapulothoracic motion for painful glenohumeral motion. This is important to note as RSA patients are also CTA patients, and they may possess altered scapular motion. Quantifying and modeling this altered scapular motion is necessary for calculating correct range of motion values, and indirectly, determining how best to avoid scapular impingement and scapular notching.

Overall, this model has been shown to be able to calculate adduction deficit for different implantation techniques. Studying adduction deficit is critical to understanding scapular notching. By understanding how lateralizing the glenosphere influences scapular impingement, clinical decisions can be made to determine how best to treat the patient

Convergence Study Test

The results of the convergence study indicate that a sparse mesh can be utilized to determine range of motion, as the least dense mesh calculated impingement at the same angle as the more dense meshes. However, a more dense mesh is required to accurately calculate contact pressure. The 267,753 and 419,733 element meshes were found to calculate maximum contact stress values within 2% of one another. Therefore, for contact pressure studies, mesh densities similar to the 267,753 element mesh should be utilized.
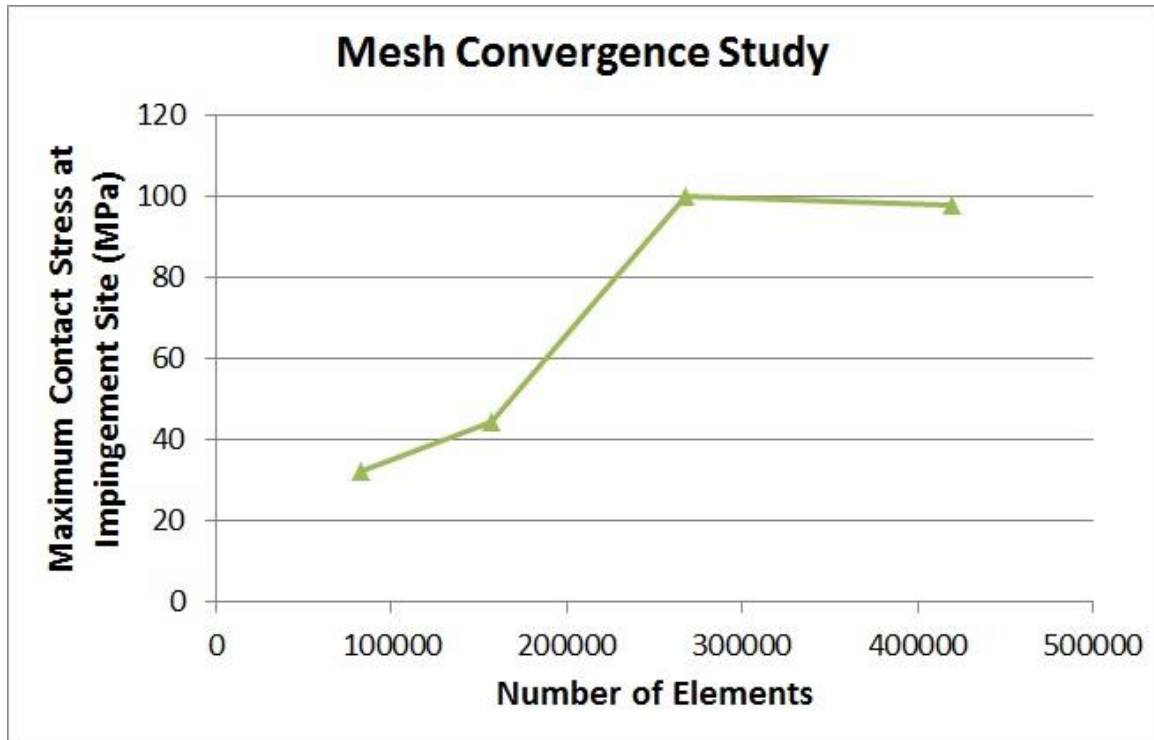
Figure 4-10 Mesh convergence study results. The two more dense meshes calculated very similar maximum contact stress values at the impingement site. The results indicate that convergence for maximum contact stress at the impingement site occurs near 267,753 elements.

Muscle Force Test

Muscle cable positioning directly affects muscle force data. This is fairly obvious; the primary reason that requisite muscle force increased with lateralization was due to the decrease in the mechanical advantage of the deltoid cable. The geometry of the cable remained constant while the center of rotation of the glenosphere moved laterally, decreasing the effective moment arm of the deltoid cable.

Current position of the cables is based on SIMM data, but more exact positioning will likely be required in future work. Before this model was developed, preliminary work with the anatomic model incorporated all three deltoid cables exactly as they are in the SIMM model. A muscle force test was performed to determine if Abaqus can be used

to determine the muscle forces of all three cables. However, only two cables recorded any force. Abaqus essentially found the least complex loading solution necessary to create stability, resulting in a non-physiologic condition. This was expected as no muscle optimization algorithm was introduced to the model. Although this model can be used currently to estimate muscle force, future models with muscle optimization using OpenSim are the next step forward.
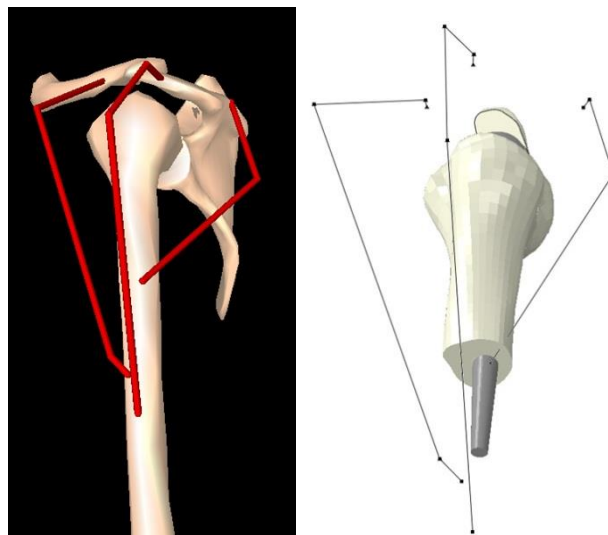
Figure 4-11 Lateral view of SIMM model (left) and preliminary Abaqus model (right). The position of the muscle cables were transferred directly from the SIMM model to the Abaqus FE model. The muscle force test was conducted. However, the forces were only recorded in two of the cables, with the majority of the load carried by the middle deltoid cable, and a stabilizing load carried by the posterior deltoid cable.

CHAPTER 5

GENERAL DISCUSSION AND FUTURE WORK

Assets of the Current RSA Model

Overall, the goal of this project was to develop a finite element model to study scapular notching, specifically the mechanical effects of changing the center of rotation of the joint and how that would relate to risk of notching. Currently, the model has the capability to provide data about impingement-free range of motion and deltoid muscle force necessary to generate different arm movements. In addition, the current model definition is amenable to incorporating muscle loading conditions derived from an inverse dynamics model, by adding more slipring elements to the FE model, simulating additional muscles. By basing the FE muscle representations on the SIMM and OpenSim models, more accurate and complete loading profiles can be created. In addition, the close relationship between the muscle models and the finite element model can open up additional opportunities.

For example, using motion capture, patient kinematic data could be collected for motions determined to have the highest risk of creating scapular notching, such as internal and external rotation with the humerus in the greatest degree of adduction possible. In addition, preoperative CT scan data could be used to create patient-specific bone surfaces, postoperative CT scan may be able to create patient-specific implant position information, and preoperative MRI scans could determine the health and function of the rotator cuffs. Using this information, a patient-specific OpenSim model could be generated. The motion profiles could then be imported into OpenSim, and, using the inverse dynamic solver, muscle forces could be calculated. The muscle positions and muscle force data could then be imported into a patient bone geometry specific FE model using the slipring elements as muscle surrogates. Finally, the FE model could determine whether or not impingement occurs and how much contact stress is seen at the interface

of the humeral cup and inferior edge of the scapula. Using this approach, quantitative information on how to best avoid scapular notching could be ascertained.

Another asset of the model is the addition of parameterization using TrueGrid. Currently, the humeral and scapular meshes are separated in two separate groups of text input files containing meshing commands. In the scapular mesh group, several text input files with similar structure have been developed to quickly generate all of the various glenosphere lateralization models with minimal effort. This model parameterization allows for rapid generation of different mesh geometries. Using the same base file, several mesh geometries can be created by redefining a parameter such as BIO length, glenosphere size, or glenosphere position. Using this command file based approach for mesh generation, many different types of lateralization and humeral cup geometry can be studied with little meshing effort required. In the future, this parametric meshing paradigm can be used to study implant variables such as humeral neck-shaft angle, stem length, humeral cup conformity, humeral cup lip height, and surgical implantation variables such as humeral retroversion and glenosphere position. In addition, the definition of the mesh geometry allows for rapid regeneration of the models in different configurations, such as patient-specific bone positions.

Future planned development of the FE model includes definition of a more complete shoulder musculature. While the deltoid is of critical importance for arm movement in patients with RSA, defining a greater number of muscles can help more realistically simulate complex arm motions. Previous attempts at incorporating multiple muscles, discussed in Chapter 4, created irregular motions when controlling the cables with loading control. This result prompted creation of the muscle force test with three deltoid cables. However, the slipring element system computed the most efficient method to bear the load by minimizing redundancy, which is contrary to the musculature of the human body in which the muscle load is shared among muscles to minimize overloading of one muscle. Conversely, Abaqus/Explicit created a loading condition in which the

cable with the best mechanical advantage was loading maximally, and the muscle required to prevent rotation was loaded with enough force to create static equilibrium. In the FE models with 3 deltoid branches modeled, the majority of the force was registered by the middle deltoid branch. The middle deltoid runs slightly anterior, creating a slight anterior or forward elevation rotation. The posterior deltoid branch helped achieve stability by restraining forward elevation rotation and registered small reaction forces to create stability. The anterior deltoid branch was not required to achieve equilibrium and did not register a load.

Therefore, future use of muscle requires accurate muscle force data generated in OpenSim from either simple motion curves or motion capture data. The current SIMM and OpenSim models are capable of calculating peak isometric muscle values. However, motion data must be incorporated into the model to generate appropriate muscle loads for motion generation. Currently, the companion OpenSim RSA model needs some development work to generate muscle forces and positions for a given motion data set. Tasks include defining mass, center of mass, and moments of inertia values for all bone segments modeled including the clavicle, scapula, and humerus. When fully defined motion or load profiles are acquired, a greater number of muscles can be introduced to the current finite element model using load control.

With greater musculature definition, greater implant stability should occur. In the OpenSim model, no capsule or ligament elements are modeled. Because of this, the use of slipring elements to approximate the capsule should not be necessary. The inverse dynamics solver in OpenSim solves the dynamics equations with only muscle elements, and the finite element software should only need muscle elements to achieve stable motion. In addition to improved muscle modeling, future versions of the RSA FE model require a better definition of scapular motion in the RSA patient population, as discussed in Chapter 4. More scapular motion occurs in the RSA shoulder as opposed to the healthy shoulder [78]. Currently, the motion of the scapula is prescribed using healthy shoulder

rhythm data from the SIMM model and the knowledge of the humeral movement through previous Abaqus/Explicit jobs. Though the values are reasonable, the prescription of scapular motion would potentially be more realistic if it was based on RSA patient data and if it was driven by a feedback loop governing scapular motion as a function of the current position of the humerus. However, preliminary attempts at creating this type of automation produced circular relationships. The position of the humerus is defined with relation to the position of the scapula. However, in the SIMM data and most literature, the rotation of the scapula is defined by the degree of humeral rotation [79-82]. Because of this, a clear algorithm for tying the motion of the scapula to the motion of the humerus is not known. At this stage, the answer is not yet clear without generating an infinite loop of self-dependencies.

Reverse Shoulder Bench-top and Cadaveric Models

To ensure that stress, muscle force, and range of motion data calculated by the finite models are accurate, the models will need to be validated against direct physical or clinical measurements. Literature models were consulted in order to create a sound validation protocol and to gain insight into the nature of current RSA validations. A model studying abduction range of motion was published by Gutierrez et al. in 2008. In that work, physical models of different implantations were created using Sawbones scapulae and plastic implant components. These configurations were used to investigate factors such as lateralization, superior/inferior implantation position, neck-shaft angle, and glenosphere diameter. The authors concluded the best implantation for range of motion involved greater lateral offsets (5 or 10 mm), inferior placement, and a 130° neck-shaft angle. Glenosphere diameter was found to have little effect on increasing range of motion [77].

In 2009, Chou et al. published a study studying the effect of different glenosphere types on scapular plane abduction range of motion. They tested four implant types of the

Lima SMR Reverse HP system (Lima Corporate, Udine, Italy): 36 mm concentric, 36 mm eccentric, 44 mm concentric and 44 mm eccentric implant geometries were studied. The concentric glenosphere were hemispherical while the eccentric glenosphere design wrapped around the scapula on the inferior edge. The humeral implant underwent a scapular plane abduction arc while attached to a coordinate measurement machine. The study found that the 44 mm eccentric glenosphere of the SMR had the best range of motion, and the 36 mm concentric having the worst [40].

In 2010, Kwon et al. studied shoulder elevation forces using a cadaveric model in which a cable simulating the deltoid muscles lifted the humerus. That study found peak glenosphere reaction forces occurred at 60° in RSA versus 90° in the native shoulder, which is similar to the FE results reported by Ahir et al. in 2004 [83].

In 2011, Ackland et al. published on a cadaveric model studying the change in joint reaction forces before and after RSA. Eight cadaveric shoulders were dissected; the muscles were replaced with cables and pulleys directed in the correct lines of action. The shoulder was implanted with the Zimmer Reverse Shoulder System (RSS) (Zimmer, Warsaw, Indiana). Joint reaction force was recorded at 0, 30, 60, 90, and 120° of scapular plane abduction for the native and Zimmer RSS. The study found RSA shoulders required less deltoid muscle force, experienced less joint contact forces, but also experience greater shear forces than native shoulders[84].

In 2012, Henninger et al. published a study using a cadaveric model to test the effect of lateralization on adduction deficit. The shoulder was implanted with a Tornier Aequalis RSA with different lateral offsets and installed into a biomechanical shoulder simulator. The reported results showed that lateral offset had no effect on adduction deficit, but increased deltoid force required an improved joint stability [85] The previous results are contradictory to other studies published where lateral offset was found to have no effect on adduction deficit. However the authors mention that the soft tissue, such as the deltoid muscle in their cadaveric specimens, may have influenced the adduction

deficit values. This indicates that the adduction deficit was not created by bony impingement but by soft tissue tension.

It is clear from the literature that many advanced RSA cadaveric studies have been created. Building upon this knowledge base, a fairly rigorous cadaveric validation can be designed for any finite element model created.
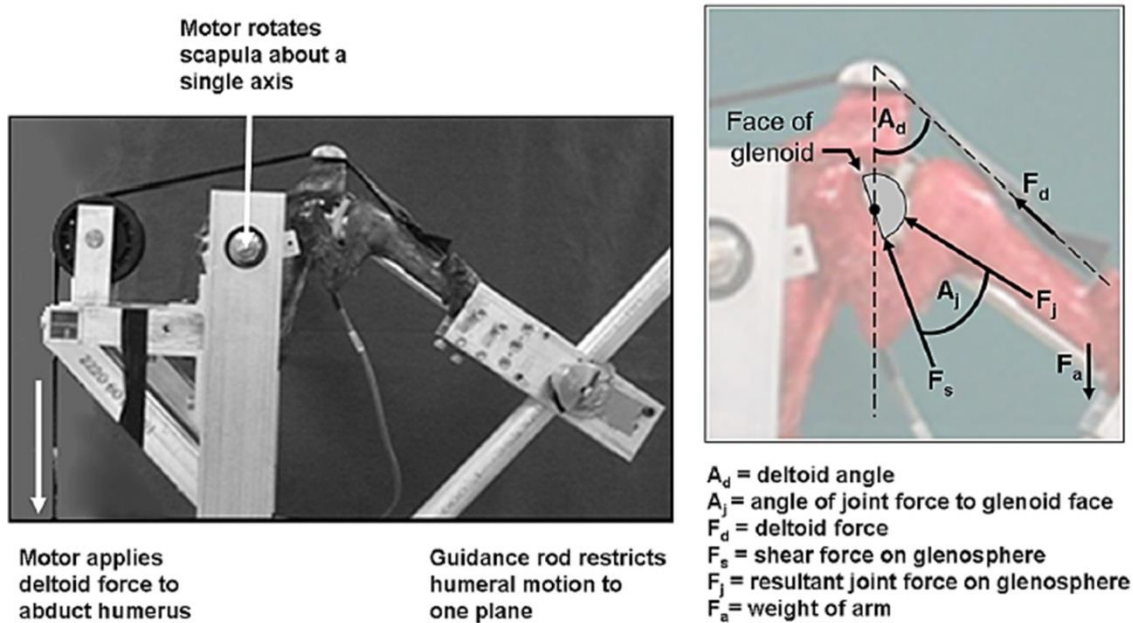
Figure 5-1 Experimental cadaveric model setup described in Kwon et al 2010. A motor rotates the scapula about a fixed axis to provide scapular motion, and another motor applies forces through a cable to create abduction. The humerus was also fixed to rotate in the frontal plane.
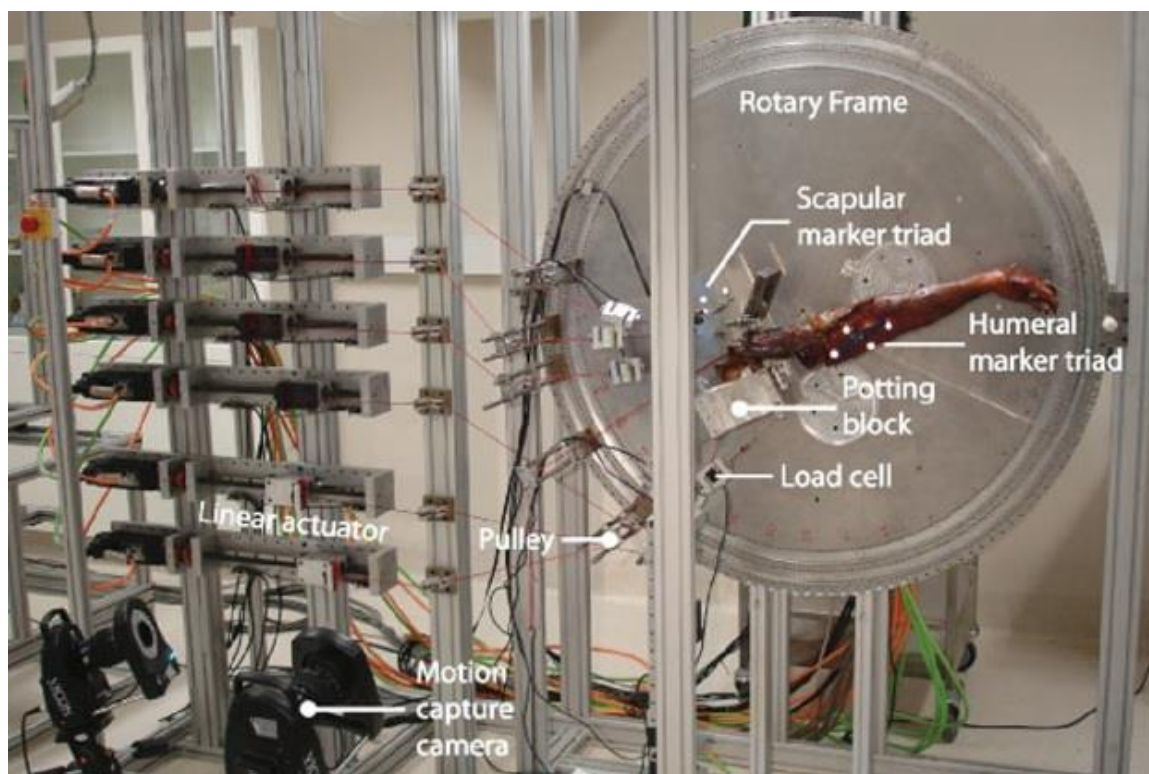
Figure 5-2 Experimental set-up of cadaveric study from (Ackland et al. 2011). Each muscle group was replaced by a cable and pulley system controlled by linear actuator. The scapula was attached to a rotary frame to control scapular rotation during motion.

Proposed Validation Strategy

Of primary interest to this work would be validation of the impingement angle (adduction deficit) and the muscle force required to adduct the arm in the scapular plane, though many other outcomes can be tested such as contact pressure at the interface between the humeral cup and inferior scapular ridge at impingement. In order to test these measures, a potential approach would be to use a cadaveric model similar to those previously reported. Using cadaveric model geometry obtained with a series of CT images, a new scapula bone surface would be used to generate a new RSA finite element model exactly replicating the physical anatomy, and a companion SIMM model could be

generated. Using the cadaver-specific SIMM model, the finite element model could be placed in the correct anatomic position, creating a cadaver specific FE model.

In order to study different amounts of lateralization, a device or faux glenosphere would need to be engineered. This device would ideally be able to accommodate every 2.5 mm of lateralization, as well as possibly incorporating frontal plane angle adjustment to study inferior tilt. This design could be as simple as a glenosphere with the capability of snapping to the baseplate with several lateralization discs able to be snapped behind the glenosphere. The device could also incorporate the existing screw that exists in the Tornier Aequalis system to provide fixation to the lateralization discs. The cadaveric model would undergo a full RSA after CT images were taken to prevent any metal artifact from occurring in the images. Finally, some device would need to be designed to provide scapular motion linked to the position of the humerus. Musculature of the rotator cuff and deltoid muscles would be dissected with the origins and insertions carefully recorded. The muscles could then be replaced with cables connected to the origins and insertions, and controlled using linear actuators. Cadaveric simulations with similar protocols were published in Kwon et al., Ackland et al., and Henninger et al. [83-85].

The impingement angle for several implantations could be determined by adducting the arm using linear actuators to control the arm position. Also, in order to get a complete three dimensional representation of the range of motion, adduction range of motion would be tested in multiple planes. Discussed in Chapter 4 results, the plane in which the motion is modeled affects the range of motion calculated, and multiple planes are required to determine the functional range of motion of clinical subjects. To ensure maximum accuracy as well as recording these planes of the impingement, some form of motion tracking would be required. Using the motion tracking data, the impingement angle would be tested against the impingement angle found by the computational model.

To test the accuracy of the muscle test, a load comparable to the muscle forces recorded in the clinic (7-17 pounds) would be applied at the wrist. Using the linear

actuators to control the musculature, the forces predicted by the OpenSim model would be applied. Then, the angular acceleration of the arm will be measured using the motion tracking setup. If the model is accurate, minimal or no motion of the arm will occur. Using this validation protocol, the ability of the current model to estimate and predict muscle forces and impingement angles could be assessed.

In addition, the stress values calculated in the finite element model could be compared to the physical model. Using TekScan (TekScan Inc., South Boston, MA) pressure sensors, contact stress values from interface between the glenosphere and humeral component could be collected using total hip arthroplasty sensors available in the Orthopaedic Biomechanics Research Laboratory. In addition, stress readings at the impingement site would be desired. However, no specific commercial sensors exist for the inferior aspect of the scapula. A generic rectangular sensor could be utilized. In order to gain confidence in stress collection, more experimentation with the sensors and cadaveric bone tissue is required.

Conclusion

In summary, a finite element model to study scapular notching in reverse shoulder arthroplasty was created. The model was created using Visible Female scapular and humeral bone segmented surfaces and Tornier Aequalis RSA glenosphere and humeral implant geometry. A SIMM inverse dynamics model was used to guide anatomic positioning of the implant and bone meshes. Finally, scapular rotation was incorporated into the model to create more realistic range of motion values. The primary factor studied was the effects of glenosphere lateralization on mechanical advantage of the deltoid muscle as well as its efficacy at eliminating scapular notching by increasing range of motion in the scapular plane. For fixed scapula models, implant lateralization was found to decrease impingement angle but also increase the deltoid force required to resist an adduction torque. However, rotating scapula models found no impingement to occur for

scapular plane adduction in models with greater than 2.5 mm of lateralization. These results illustrate the importance of understanding the effects of implant lateralization on scapular notching.

In addition, this model has been developed to complement an inverse dynamics model. This feature allows straightforward transfer of muscle positioning data from the inverse dynamics model to the finite element model. Future plans include creating more muscle slipring elements in the finite element model, utilizing motion capture of internal and external rotation to create muscle load data in OpenSim, and using the muscle force data to model contact stress on the interface between the humeral cup and inferior edge of the scapula. In addition, a detailed validation is planned to verify the accuracy of all previous results.

REFERENCES

1.   Hall, S.J., *Basic Biomechanics*. 5 ed. 2007, New York, NY: McGraw-Hill. 544.

2.   O'Brien, S.J., et al., *The anatomy and histology of the inferior glenohumeral ligament complex of the shoulder.* Am J Sports Med, 1990. **18**(5): p. 449-56.

3.   Warner, J.J., et al., *Static capsuloligamentous restraints to superior-inferior translation of the glenohumeral joint.* Am J Sports Med, 1992. **20**(6): p. 675-85.

4.   Steinbeck, J., U. Liljenqvist, and J. Jerosch, *The anatomy of the glenohumeral ligamentous complex and its contribution to anterior shoulder stability.* J Shoulder Elbow Surg, 1998. **7**(2): p. 122-6.

5.   *Picture of the Shoulder*. Pain Management Health Center [Webpage] 2010 [cited 2014 March 20th]; Available from: http://www.webmd.com/pain-management/picture-of-the-shoulder.

6.   Inman, V.T., J.B. Saunders, and L.C. Abbott, *Observations of the function of the shoulder joint. 1944.* Clin Orthop Relat Res, 1996(330): p. 3-12.

7.   Tempelhof, S., S. Rupp, and R. Seil, *Age-related prevalence of rotator cuff tears in asymptomatic shoulders.* J Shoulder Elbow Surg, 1999. **8**(4): p. 296-9.

8.   Sher, J.S., et al., *Abnormal findings on magnetic resonance images of asymptomatic shoulders.* J Bone Joint Surg Am, 1995. **77**(1): p. 10-5.

9.   Mather, R.C., 3rd, et al., *The societal and economic value of rotator cuff repair.* J Bone Joint Surg Am, 2013. **95**(22): p. 1993-2000.

10.   Neer, C.S., 2nd, E.V. Craig, and H. Fukuda, *Cuff-tear arthropathy.* J Bone Joint Surg Am, 1983. **65**(9): p. 1232-44.

11.   Nam, D., et al., *Rotator cuff tear arthropathy: evaluation, diagnosis, and treatment: AAOS exhibit selection.* J Bone Joint Surg Am, 2012. **94**(6): p. e34.

12.   Flatow, E.L. and A.K. Harrison, *A history of reverse total shoulder arthroplasty.* Clin Orthop Relat Res, 2011. **469**(9): p. 2432-9.

13.   Ecklund, K.J., et al., *Rotator cuff tear arthropathy.* J Am Acad Orthop Surg, 2007. **15**(6): p. 340-9.

14.   Feeley, B.T., R.A. Gallo, and E.V. Craig, *Cuff tear arthropathy: current trends in diagnosis and surgical management.* J Shoulder Elbow Surg, 2009. **18**(3): p. 484-94.

15.   Neer, C.S., 2nd, *Replacement arthroplasty for glenohumeral osteoarthritis.* J Bone Joint Surg Am, 1974. **56**(1): p. 1-13.

16.   Boileau, P., et al., *Grammont reverse prosthesis: design, rationale, and biomechanics.* J Shoulder Elbow Surg, 2005. **14**(1 Suppl S): p. 147S-161S.

17.   Nam, D., et al., *Reverse total shoulder arthroplasty: current concepts, results, and component wear analysis.* J Bone Joint Surg Am, 2010. **92 Suppl 2**: p. 23-35.

18.   Sanchez-Sotelo, J., R.H. Cofield, and C.M. Rowland, *Shoulder hemiarthroplasty for glenohumeral arthritis associated with severe rotator cuff deficiency.* J Bone Joint Surg Am, 2001. **83-A**(12): p. 1814-22.

19.   Boileau, P., et al., *Arthroplasty of the shoulder.* J Bone Joint Surg Br, 2006. **88**(5): p. 562-75.

20.   Sirveaux, F., et al., *Grammont inverted total shoulder arthroplasty in the treatment of glenohumeral osteoarthritis with massive rupture of the cuff. Results of a multicentre study of 80 shoulders.* J Bone Joint Surg Br, 2004. **86**(3): p. 388-95.

21.   Franklin, J.L., et al., *Glenoid loosening in total shoulder arthroplasty. Association with rotator cuff deficiency.* J Arthroplasty, 1988. **3**(1): p. 39-46.

22.   Wierks, C., et al., *Reverse total shoulder replacement: intraoperative and early postoperative complications.* Clin Orthop Relat Res, 2009. **467**(1): p. 225-34.

23.   Gerber, C., S.D. Pennington, and R.W. Nyffeler, *Reverse total shoulder arthroplasty.* J Am Acad Orthop Surg, 2009. **17**(5): p. 284-95.

24.   Werner, C.M., et al., *Treatment of painful pseudoparesis due to irreparable rotator cuff dysfunction with the Delta III reverse-ball-and-socket total shoulder prosthesis.* J Bone Joint Surg Am, 2005. **87**(7): p. 1476-86.

25.   Frankle, M., et al., *The reverse shoulder prosthesis for glenohumeral arthritis associated with severe rotator cuff deficiency. a minimum two-year follow-up study of sixty patients surgical technique.* J Bone Joint Surg Am, 2006. **88 Suppl 1 Pt 2**: p. 178-90.

26.   Nyffeler, R.W., et al., *Analysis of a retrieved delta III total shoulder prosthesis.* J Bone Joint Surg Br, 2004. **86**(8): p. 1187-91.

27.   Frankle, M., et al., *The Reverse Shoulder Prosthesis for glenohumeral arthritis associated with severe rotator cuff deficiency. A minimum two-year follow-up study of sixty patients.* J Bone Joint Surg Am, 2005. **87**(8): p. 1697-705.

28. Walch, G., et al., *Do the indications, results, and complications of reverse shoulder arthroplasty change with surgeon's experience?* J Shoulder Elbow Surg, 2012. **21**(11): p. 1470-7.

29. Nyffeler, R.W., C.M. Werner, and C. Gerber, *Biomechanical relevance of glenoid component positioning in the reverse Delta III total shoulder prosthesis.* J Shoulder Elbow Surg, 2005. **14**(5): p. 524-8.

30. Simovitch, R.W., et al., *Predictors of scapular notching in patients managed with the Delta III reverse total shoulder replacement.* J Bone Joint Surg Am, 2007. **89**(3): p. 588-600.

31. de Wilde, L.F., et al., *Prosthetic overhang is the most effective way to prevent scapular conflict in a reverse total shoulder prosthesis.* Acta Orthop, 2010. **81**(6): p. 719-26.

32. Van Tongel, A., et al., *Bony increased-offset reversed shoulder arthroplasty: minimizing scapular impingement while maximizing glenoid fixation.* Clin Orthop Relat Res, 2011. **469**(8): p. 2389-90; author reply 2391-2.

33. Boileau, P., et al., *Bony increased-offset reversed shoulder arthroplasty: minimizing scapular impingement while maximizing glenoid fixation.* Clin Orthop Relat Res, 2011. **469**(9): p. 2558-67.

34. Nicholson, G.P., E.J. Strauss, and S.L. Sherman, *Scapular notching: Recognition and strategies to minimize clinical impact.* Clin Orthop Relat Res, 2011. **469**(9): p. 2521-30.

35. Levigne, C., et al., *Scapular notching in reverse shoulder arthroplasty: is it important to avoid it and how?* Clin Orthop Relat Res, 2011. **469**(9): p. 2512-20.

36. Kempton, L.B., et al., *A radiographic analysis of the effects of glenosphere position on scapular notching following reverse total shoulder arthroplasty.* J Shoulder Elbow Surg, 2011. **20**(6): p. 968-74.

37. Falaise, V., et al., *Scapular notching in reverse shoulder arthroplasties: the influence of glenometaphyseal angle.* Orthop Traumatol Surg Res, 2011. **97**(6 Suppl): p. S131-7.

38. Boughebri, O., et al., *Arthroscopic dynamic analysis of scapular notching in reverse shoulder arthroplasty.* Orthop Traumatol Surg Res, 2011. **97**(8): p. 779-84.

39. Levigne, C., et al., *Scapular notching in reverse shoulder arthroplasty.* J Shoulder Elbow Surg, 2008. **17**(6): p. 925-35.

40.   Chou, J., et al., *Biomechanical evaluation of different designs of glenospheres in the SMR reverse total shoulder prosthesis: range of motion and risk of scapular notching.* J Shoulder Elbow Surg, 2009. **18**(3): p. 354-9.

41.   Bhatti, M.A., *Advanced Topics in Finite Element Analysis of Structures* 2006, Hoboken, New Jersey: John Wiley & Sons. 590.

42.   Gupta, K.K. and J.L. Meek, *A brief history of the beginning of the finite element method.* International Journal for Numerical Methods in Engineering, 1996. **39**(22): p. 3761-3774.

43.   Huiskes, R. and E.Y. Chao, *A survey of finite element analysis in orthopedic biomechanics: the first decade.* J Biomech, 1983. **16**(6): p. 385-409.

44.   Prendergast, P.J., *Finite element models in tissue mechanics and orthopaedic implant design.* Clin Biomech (Bristol, Avon), 1997. **12**(6): p. 343-366.

45.   Buchler, P., et al., *A finite element model of the shoulder: application to the comparison of normal and osteoarthritic joints.* Clin Biomech (Bristol, Avon), 2002. **17**(9-10): p. 630-9.

46.   Terrier, A., et al., *Effect of supraspinatus deficiency on humerus translation and glenohumeral contact force during abduction.* Clin Biomech (Bristol, Avon), 2007. **22**(6): p. 645-51.

47.   Ellis, B.J., et al., *Finite element modelling of the glenohumeral capsule can help assess the tested region during a clinical exam.* Comput Methods Biomech Biomed Engin, 2010. **13**(3): p. 413-8.

48.   Drury, N.J., et al., *Finding consistent strain distributions in the glenohumeral capsule between two subjects: implications for development of physical examinations.* J Biomech, 2011. **44**(4): p. 607-13.

49.   Lacroix, D., L.A. Murphy, and P.J. Prendergast, *Three-dimensional finite element analysis of glenoid replacement prostheses: a comparison of keeled and pegged anchorage systems.* J Biomech Eng, 2000. **122**(4): p. 430-6.

50.   Couteau, B., et al., *Finite element analysis of the mechanical behavior of a scapula implanted with a glenoid prosthesis.* Clin Biomech (Bristol, Avon), 2001. **16**(7): p. 566-75.

51.   Hopkins, A.R., U.N. Hansen, and A.A. Amis, *Finite element models of total shoulder replacement: application of boundary conditions.* Comput Methods Biomech Biomed Engin, 2005. **8**(1): p. 39-44.

52.   Hopkins, A.R., et al., *Finite element modelling of glenohumeral kinematics following total shoulder arthroplasty.* J Biomech, 2006. **39**(13): p. 2476-83.

53.   Mansat, P., et al., *Evaluation of the glenoid implant survival using a biomechanical finite element analysis: influence of the implant design, bone properties, and loading location.* J Shoulder Elbow Surg, 2007. **16**(3 Suppl): p. S79-83.

54.   Sarah, J., et al., *Failure mechanism of the all-polyethylene glenoid implant.* J Biomech, 2010. **43**(4): p. 714-9.

55.   Terrier, A., et al., *Importance of polyethylene thickness in total shoulder arthroplasty: a finite element analysis.* Clin Biomech (Bristol, Avon), 2012. **27**(5): p. 443-8.

56.   Ahir, S.P., et al., *Analysis of glenoid fixation for a reversed anatomy fixed-fulcrum shoulder replacement.* J Biomech, 2004. **37**(11): p. 1699-708.

57.   Terrier, A., et al., *Simulated joint and muscle forces in reversed and anatomic shoulder prostheses.* J Bone Joint Surg Br, 2008. **90**(6): p. 751-6.

58.   Yang, C.C., et al., *Stress analysis of glenoid component in design of reverse shoulder prosthesis using finite element method.* J Shoulder Elbow Surg, 2013. **22**(7): p. 932-9.

59.   Virani, N.A., et al., *In vitro and finite element analysis of glenoid bone/baseplate interaction in the reverse shoulder design.* J Shoulder Elbow Surg, 2008. **17**(3): p. 509-21.

60.   Gutierrez, S., et al., *Range of impingement-free abduction and adduction deficit after reverse shoulder arthroplasty. Hierarchy of surgical and implant-design-related factors.* J Bone Joint Surg Am, 2008. **90**(12): p. 2606-15.

61.   Kontaxis, A. and G.R. Johnson, *The biomechanics of reverse anatomy shoulder replacement--a modelling study.* Clin Biomech (Bristol, Avon), 2009. **24**(3): p. 254-60.

62.   Gulotta, L.V., et al., *Humeral component retroversion in reverse total shoulder arthroplasty: a biomechanical study.* J Shoulder Elbow Surg, 2012. **21**(9): p. 1121-7.

63.   Terrier, A., et al., *Activities of daily living with reverse prostheses: importance of scapular compensation for functional mobility of the shoulder.* J Shoulder Elbow Surg, 2013. **22**(7): p. 948-53.

64.   Hoenecke, H.R., Jr., C. Flores-Hernandez, and D.D. D'Lima, *Reverse total shoulder arthroplasty component center of rotation affects muscle function.* J Shoulder Elbow Surg, 2014.

65.   Walch, G., *Aequalis Reversed Shoulder with BIO-RSA Live Surgery June 18, 2010*. 2012, Tornier Inc.

66.   Elkins, J.M., et al., *Morbid obesity may increase dislocation in total hip patients: a biomechanical analysis.* Clin Orthop Relat Res, 2013. **471**(3): p. 971-80.

67.   Elkins, J.M., et al., *The capsule's contribution to total hip construct stability--a finite element analysis.* J Orthop Res, 2011. **29**(11): p. 1642-8.

68.   *UHMWPE (ultrahigh molecular weight polyethylene)*. Technical Product Data Sheets [Web Page] [cited 2013; Available from: www.plastic-products.com/spec11.htm.

69.   Terrier, A., et al., *Comparison of polyethylene wear in anatomical and reversed shoulder prostheses.* J Bone Joint Surg Br, 2009. **91**(7): p. 977-82.

70.   Chaffin, D.B., Andersson, Gunnar B.J., Martin, Bernard, J. Martin, *Occupational Biomechanics*. 4th ed. 2006, Hoboken, New Jersey: Wiley-Interscience.

71.   *31.1.5 Connection-type library*. Abaqus Analysis User's Manual [Web Page] 2012 [cited 2014 4/28/2014]; Available from: http://www.tu-chemnitz.de/projekt/abq_hilfe/docs/v6.12/books/usb/default.htm?startat=pt06ch31s02alm28.html#usb-elm-econnectorbehavior.

72.   Weiss, J.A. and J.C. Gardiner, *Computational modeling of ligament mechanics.* Crit Rev Biomed Eng, 2001. **29**(3): p. 303-71.

73.   Garner, B.A. and M.G. Pandy, *Estimation of musculotendon properties in the human upper limb.* Ann Biomed Eng, 2003. **31**(2): p. 207-20.

74.   Cote, M.P., et al., *Reference values for physical performance measures in the aging working population.* Hum Factors, 2014. **56**(1): p. 228-42.

75.   Hamberg-van Reenen, H.H., et al., *Age-related differences in muscular capacity among workers.* Int Arch Occup Environ Health, 2009. **82**(9): p. 1115-21.

76.   Holzbaur, K.R., W.M. Murray, and S.L. Delp, *A model of the upper extremity for simulating musculoskeletal surgery and analyzing neuromuscular control.* Ann Biomed Eng, 2005. **33**(6): p. 829-40.

77.   Gutierrez, S., et al., *Evaluation of abduction range of motion and avoidance of inferior scapular impingement in a reverse shoulder model.* J Shoulder Elbow Surg, 2008. **17**(4): p. 608-15.

78.   Scibek, J.S., J.E. Carpenter, and R.E. Hughes, *Rotator cuff tear pain and tear size and scapulohumeral rhythm.* J Athl Train, 2009. **44**(2): p. 148-59.

79.   Amasay, T. and A.R. Karduna, *Scapular kinematics in constrained and functional upper extremity movements.* J Orthop Sports Phys Ther, 2009. **39**(8): p. 618-27.

80.   Ebaugh, D.D., P.W. McClure, and A.R. Karduna, *Scapulothoracic and glenohumeral kinematics following an external rotation fatigue protocol.* J Orthop Sports Phys Ther, 2006. **36**(8): p. 557-71.

81.   Ebaugh, D.D., P.W. McClure, and A.R. Karduna, *Three-dimensional scapulothoracic motion during active and passive arm elevation.* Clin Biomech (Bristol, Avon), 2005. **20**(7): p. 700-9.

82.   McClure, P.W., et al., *Direct 3-dimensional measurement of scapular kinematics during dynamic movements in vivo.* J Shoulder Elbow Surg, 2001. **10**(3): p. 269-77.

83.   Kwon, Y.W., et al., *Analysis of reverse total shoulder joint forces and glenoid fixation.* Bull NYU Hosp Jt Dis, 2010. **68**(4): p. 273-80.

84.   Ackland, D.C., et al., *Muscle and joint-contact loading at the glenohumeral joint after reverse total shoulder arthroplasty.* J Orthop Res, 2011. **29**(12): p. 1850-8.

85.   Henninger, H.B., et al., *Effect of lateral offset center of rotation in reverse total shoulder arthroplasty: a biomechanical study.* J Shoulder Elbow Surg, 2012. **21**(9): p. 1128-35.